Institute of Thermal Turbomachinery
Prof. Dr.-Ing. H.-J. Bauer

Transient development of perturbations in a stratified turbulent shear flow

Diploma Thesis

of

Carlos Yáñez Vico

Supervisor: **Dr.-Ing. Manuel García-Villalba**

March 2008

University of Karlsruhe (TH)

Universität Karlsruhe (TH)
Institut für Thermische Strömungsmaschinen
Kaiserstraße 12
D-76131 Karlsruhe
Deutschland

Declaration

I declare that I have written this diploma thesis on my own and I did not use any supplemental sources or material not mentioned. I agree that my report is copied or presented in a library.

Hiermit versichere ich die vorliegende Diplomarbeit selbständig verfasst und keine weiteren als die angegebenen Quellen und Hilfsmittel benutzt zu haben. Ich erkläre mich damit einverstanden, dass meine Arbeit in eine Bibliothek eingestellt oder kopiert wird.

Karlsruhe, March 2008

Contents

List of figures

List of tables

Nomenclature

Roman

a_n	coefficients of the Chebyshev expansion	-
c	phase speed	m/s
G	maximum energy amplification	-
h	semi-height of the channel	m
k	spatial wave number	$1/m$
P	pressure	N/m^2
$\overline{P}$	mean pressure	N/m^2
p	perturbation pressure	N/m^2
$\hat{q}_i$	set of eigenfunctions of the linearized eigenvalue problem	-
Re	Reynolds number	-
Re_τ	friction Reynolds number	-
Ri	Richardson number	-
T_n	polynomials of the Chebyshev expansion	-
U_i	velocity in the xi-direction (U_1 = U, U_2 = V, U_3 = W)	m/s
$\overline{U}_i$	mean velocity vector ($\overline{U}_1 = \overline{U}$, $\overline{U}_2 = \overline{V}$, $\overline{U}_3 = \overline{W}$)	m/s
u_i	perturbation velocity vector (u_1 = u, u_2 = v, u_3 = w)	m/s
U_b	bulk velocity	m/s
U_c	velocity in the middle of the channel	m/s
u_τ	friction velocity	m/s
x_i	basis coordinate system (x_1 = x, x_2 = y, x_3 =z)	m

Greek

α	streamwise wave number	$1/m$
β	spanwise wave number	$1/m$
δ_v	viscous lengthscale	m
η	normal vorticity	$1/s$
λ_x	streamwise wavelength	m
λ_z	spanwise wavelength	m
ρ	density	kg/m^3
σ_1	principal singular value	-
τ_w	wall shear stress	N/m^2
υ	kinematic viscosity	m^2/s
υ_t	turbulent kinematic viscosity	m^2/s
ω	frequency	$1/s$

Operators and Symbols

f'	derivative of the function in the normal direction	
f^+	function f normalised with the viscous lengthscale	
$\partial/\partial x_i \equiv \partial_i$	spatial derivative in the i direction	$1/m$
$\partial/\partial t \equiv \partial_t$	partial derivative in time	$1/s$

Chapter 1.- Introduction

Stratified turbulent shear flows occur especially in many applications in environmental engineering and geophysics, but also in aeronautical and industrial engineering. These flows are characterized by the variation of fluid density in vertical direction that can result in qualitative and quantitative modifications of the flow patterns by buoyancy (Turner, 1973). Stable stratification suppresses vertical mixing and momentum. However, a stably stratified fluid can support internal waves, instabilities and turbulence that are critical in transport and mixing.

In the aeronautical field stratified flows play an increasing important role in the development of turbomachinery. Considerable progress in application of computational fluid dynamics (CFD) for aeroengine internal flow systems has been made in recent years. However, there are a number of flow phenomena that are not yet fully understood, and that are directly linked to stratification. These include buoyancy-affected flows in rotating cavities and mixed air/oil flows (Chew & Hills 2007 and Tucker 2007). Co-rotating disc cavities occur in HP compressors in which disc rims are generally hotter than the disc cobs, which are cooled by a central axial throughflow. The positive radial temperature gradient (that is to say, the density gradient) results in strong buoyancy effects in the centripetal force field. The resulting flows have been known to be strongly tree-dimensional and unsteady for some time and have been recognized as particularly challenging for CFD.

Stratified flows are also common in the atmosphere and in the oceans. The ocean is predominantly subject to stable stratification which, under external excitation, supports an environment of internal waves which may then break and generate turbulence (Thorpe, 2005). Turbulence in the ocean is responsible for upward transport of bottom water, nutrients, biological species, etc. In the atmosphere, stratification affects, for example, the transport of pollutants released at ground level.

Although much progress has been made toward understanding the excitation of gravity waves and the interaction between gravity waves and their background flow, many questions remain. Observations of turbulence in geophysical flows show that in the presence of stratification, turbulence is highly intermittent and organized in local regions of convective overturning called ‘patches’. Microstructure in stratified flows seems to result from early decay of transitional structures that collapse convectively before maturing into turbulence. Identification of processes that lead to local convective overturning in stratified flows is therefore of considerable importance. In this study the transient development of perturbations in a stratified turbulent shear flow is investigated. The modes with the largest transient growth could be related to the large structures observed in real flows.

This is achieved through the analysis of the temporal stability of the linearized Navier-Stokes equations using the Boussinesq approximation (Kundu & Cohen, 2002). In order to be able to consider turbulent base flows, eddy viscosity and eddy diffusivity approximations are employed. The obtained results are compared to DNS data.

A code in Matlab has been developed to solve the temporal stability problem. In order to validate this code, validations have been made comparing results of simpler cases to the ones in the literature. Three main steps of validation have been carried out solving the laminar and turbulent problems both without stratification and the laminar and stratified case.

The work is divided into four chapters. In the first chapter an introduction is given to the treatment of the transient growth with the linearized Navier-Stokes equations, including the explanation of this phenomenon and the computational procedures used in the present work. The second chapter describes the different steps of validation, highlighting some important results. In the third chapter, the results of the complete problem are presented, compared to the DNS data and discussed. This thesis ends with a conclusion and recommendation for further work.

1.1 Principles of Transient Growth

Linear stability analysis is a standard tool for studying the stability of many flow problems, in particular of viscous channel flows (Drazing and Reid 1981). It involves examining the evolution of small perturbations by linearizing the Navier-Stokes equations and yields the Orr-Sommerfeld (O-S) and Squire (Sq) equations. Stability is then determined by examining the O-S and Sq eigenvalues. If there is an eigenvalue in the upper half-plane, then there is an exponentially growing mode and the flow is said to be linearly unstable. This analysis, for the laminar and non-stratified case, has been carried out using both analytical and numerical techniques. The results say that Poiseuille flow is linearly stable if the Reynolds number Re is less than Rc ≈ 5772 (Orszag 1971).

However, these results from linear theory do not agree with experimental studies, which show that Poiseuille flow may become unstable at Reynolds numbers as low as Re ≈ 1000 (Patel and Head 1969).

A possible explanation comes from linear stability, through the concept of algebraic growth. Although the eigenvalues of the O-S and Sq equations are damped, which means that the energy of small perturbations decay to zero as $t \rightarrow \infty$ (the flow is linearly stable), it may occur that in the initial times an amplification of the energy, transient growth, happens. This growth occurs in the absence of nonlinear effects and it is explained by the non-orthogonality of the O-S eigenfunctions (Schmid & Henningson, 2001). In mathematical terms, growth occurs because the Orr-Sommerfeld operator, which is related to the Orr-Sommerfel equation, is non-normal. For three-dimensional perturbations, growth by a factor *O*(1000) can occur (Gustavsson 1991; Butler and Farrel 1992).

A simple example can illustrate how this non-orthogonality of the O-S eigenfunctions can produce the transient growth. Two eigenfunctions are, for example, the solution of a stable initial value problem and each of them has a different damping rate, which is characterized by its corresponding eigenvalue. As $t \rightarrow \infty$ the perturbation decays to zero, but it may happen that due to enough differences in their damping rates, the total perturbation, which is a combination of the two eigenfunctions, grows initially. Figure 1.1 shows this fact.

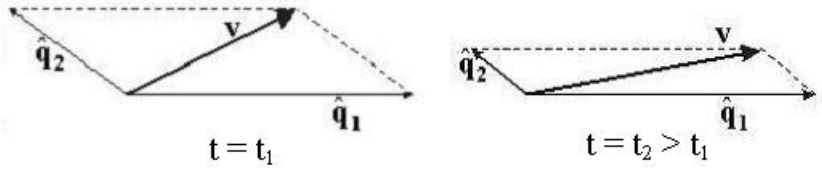

Figure 1-1: Non-orthogonality of the O-S eigenfunctions as the responsible of transient growth in a stable configuration. Figure adapted from Schmid & Henningson (2001)

In a laminar flow, linear stability analysis predicts a necessary Reynolds number at which the flow become linearly unstable higher than what experiments show. At this point, a possible explanation is given by transient growth, which is still based on linear theory, as it has been noted above. For lower values of Re than the first unstable one, there is energy amplification due to the non-orthogonality of the damped O-S and Squire eigenfunctions (this is a linear effect). Then, the magnitude of this energy growth can be sufficient to produce turbulent transition or to induce non-linear effects (since the perturbation has grown in energy so much that can no longer be considered small) that yield a turbulent state.

With a stable turbulent profile, the concept of transient growth let us determine the energy amplification that reaches a perturbation of concrete size. Thus, the most amplified solutions point out the organization of turbulent structures in actual channels, as the agreement with experiments and DNS shows (see section 2.2 and Del Álamo & Jiménez 2006)

1.2 Geometry and Governing Parameters

The model of a channel flow consists in a flow between two infinite plates whose velocity is dominant in a direction parallel to these plates, which is taken as the x-axis (streamwise direction). A Cartesian coordinate system is used with normal basis (x,y,z) which corresponds to the streamwise, wall-normal and spanwise direction respectively. A diagram of this model is represented in Figure 1-2.

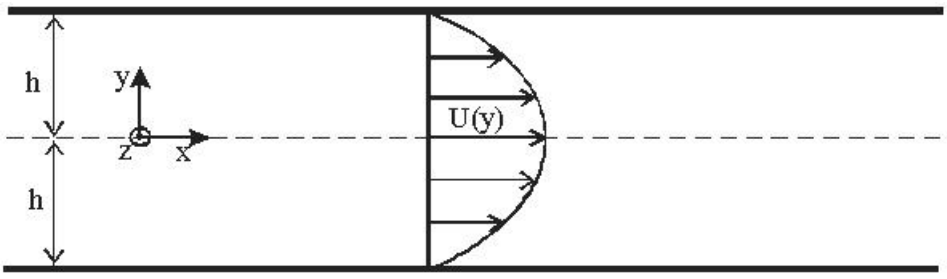

Figure 1-2: Channel flow geometry and coordinate sytem.

The treatment of fluid as a continuous medium is generally accepted to be valid also for turbulent flows. The equations for conservation of mass and momentum derived by this fundamental assumption are known as the Navier-Stokes equations (Batchelor 1967).

In order to be able to generalize the results of this work, the Navier-Stokes equations are solved in a dimensionless form. Therefore, every quantity is normalized by characteristic scaling parameters,

$$x^* = x/h,\ U^* = U/U_c,\quad t^* = t/\left(h/U_c\right),\quad p^* = p/\left(\rho_0 U_c^2\right), \tag{1.1}$$

where U_c is the mean velocity in the middle of the channel and h the semi-height of the channel. Using the scaling parameters, the momentum equation for a non-stratified problem can be written in a dimensionless form, where there is only one parameter remaining important, namely the Reynolds number, whose definition:

$$\mathrm{Re} = \frac{U_c h}{\upsilon} \tag{1.2}$$

This Reynolds number similarity is an important property of the Navier-Stokes equation, as it makes experiments comparable over a range of different length scales, provided that their velocities are appropriately scaled.

The Reynolds number can be seen as the ratio of convection and diffusion. Hence, it is a direct indicator of the intensity of diffusion present in the flow. This has an important effect on the fluid behaviour: At low Reynolds numbers, diffusion is strong and thus damps out small perturbations. As a result, the streamlines are smooth and the flow is laminar. With increasing Reynolds number the stabilizing effect reduces and after reaching a certain value the flow becomes chaotic in the sense that the effect of a small change, for example in the boundary conditions, cannot be predicted after a certain time in the future.

When the momentum equation for a stratified flow is written in a dimensionless form, another parameter, apart from the Reynolds number, appears. This is the Richardson number. Both, the Reynolds and the Richardson number, are the parameters that characterize the flow and that make experiments comparable. Two definitions of the Richardson number are used in this study in order to be coherent with the literature taken to compare with. The difference between them lies on the velocity used to normalize, the mean velocity in the centre of the channel, U_c, or the friction velocity u_τ[1].

$$Ri_c = \frac{\Delta\rho\, g\, h}{\rho_0 U_c^2}; \qquad Ri_\tau = \frac{\Delta\rho\, g\, h}{\rho_0 u_\tau^2} \qquad \Rightarrow \qquad Ri_c = \left(\frac{U_c}{u_\tau}\right)^2 Ri_\tau \tag{1.3}$$

Ri_τ	(U_c/u_τ)	Ri_c
60	23.58	0.1079
120	29.68	0.1362
480	43.38	0.2551

Table 1-1: Comparison of the two definitions of the Richardson number adopted in this study. The values of (U_c/u_τ) are taken from the mean velocity model used in Chapter 3

The last parameter involved in the equations (specifically in the energy equation) is the Prandtl number, which is a dimensionless number approximating the ratio of momentum diffusivity (kinematic viscosity) and thermal diffusivity.

$$\mathrm{Pr} = \frac{\upsilon}{\alpha} = \frac{\textit{viscous diffusion rate}}{\textit{thermal diffusion rate}} = \frac{\mu c_p}{k} \tag{1.4}$$

where υ is the kinematic viscosity (SI units : m^2/s), α the thermal diffusivity (SI units: m^2/s), μ the viscosity (SI units: Pa s) k thermal conductivity (SI units: W/(mK)) and c_p the specific heat (SI units: J/(kg K)) . Throughout this study the value of the Prandtl number taken is 0.7 that corresponds to the typical value of the air and many other gases.

[1] Friction velocity is defined as $u_\tau \equiv \sqrt{\tau_w/\rho}$ where τ_w is the wall shear stress $\tau_w \equiv \rho\upsilon\left(\frac{dU}{dy}\right)_{y=0}$

1.3 Effects of stratification on shear flows.

In this work stratified flow will be called to a flow which has a density distribution that varies along the vertical direction but is constant in horizontal planes. It is considered within this thesis that density changes smoothly, that is to say, the mean density distribution is continous. Important effects of stratification on shear flows are buoyant convection (arising from an unstable density profile), and, turbulence and mixing, either air and oil in turbomachinery or pollutants in the enviroment, when the stratification is stable.

A flow is said to be stable when its density decreases upwards. Otherwise, stratification is unstable. This clasification is explained in terms of energy. In Figure 1-3 stable (i) and unstable (ii) stratification for linear density variation are reprensented. The potential energy in (ii) is greater than in (i). Thus, any disturbance in (ii) convert the flow state into (i), which is the situation of less energy. Indeed any mass-conserving adjustment of the density profile in (ii) will lead to a state of lower potential energy, so that any disturbance, however small, will lead to a release of potential energy.

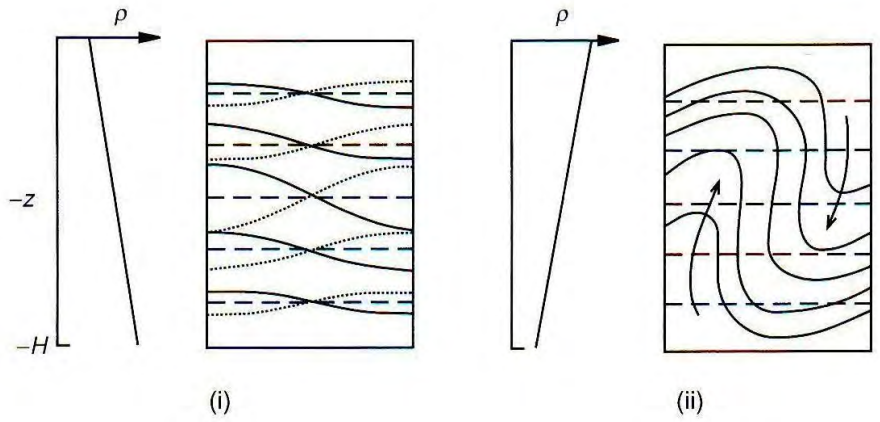

Figure 1-3: Stable (i, on left) and unstable (ii, right) stratification for a linear density variation with depth. Periodic disturbances, internal waves, are shown in (i) by full lines and dotted lines, whilst growing disturbances in (ii) are illustrated as full lines. Figure taken from Thorpe (2005)

In a stably stratified fluid in the presence of gravity, density perturbations tend to be damped by acting buoyancy forces. This generates gravity internal waves which are the oscillation of density in the bossom of the fluid and wave-like velocity field. If there is initially a sufficient energy growth, these internal waves can lead to the formation of billows that evolves into breaking themselves, described by the Kelvin-Helmholtz instability, and creating turbulence (see Figure 1-3). In a laminar situation this phenomenon causes instability and the transition to a turbulent state. In a turbulent flow it acts as another random source of keeping turbulence. A plentiful and neat description of Kelvin-Helmholtz is given in Drazin (2002). The turbulence generated gives us a better understanding on how mixing acts in stably stratified flows.

In the introduction was mentioned the concept of ‘patches’, which agrees with geophysical observations. These are local regions on the flow of convective overturning where turbulence is highly intermittent and organized. There, the stratified behaviour above commented is dominant. Considerable effort has been expended in recent years on the study of these patches, which are related to the evolution of mixing efficiency in Kelvin-Helmholtz billows (Smyth et al 2001, Caulfield and Peltier 2000, Thorpe 2005).

On the other hand, flows are statically unstable when density increases upwards. Any small perturbance changes completely the state of the fluid into another of lower energy. These unstably stratified flows are also called convective flows, in which buoyancy forces play the major role because they are the source of energy for the mean motion itself. In a continous density profile the motion it is assumed to be in the form of 'plumes'. These plumes are commonly also called buoyant jets. Detailed descriptions can be found in the literature, for example in Turner (1973)

Throughout this thesis, the tackled study is restricted to stably stratification. It is also made the assumption of Boussinesq approximation. In the Boussinesq approximation it is supposed that the effect of a variable density in the momentum of fluid particles can be neglected, although its variation in determining gravitational or bouyancy forces is non-negligible and usually essential in determining the physical processes in stratified fluids. The approximation is usually valid when small density variations are considered (this is for instance the case of the ocean).

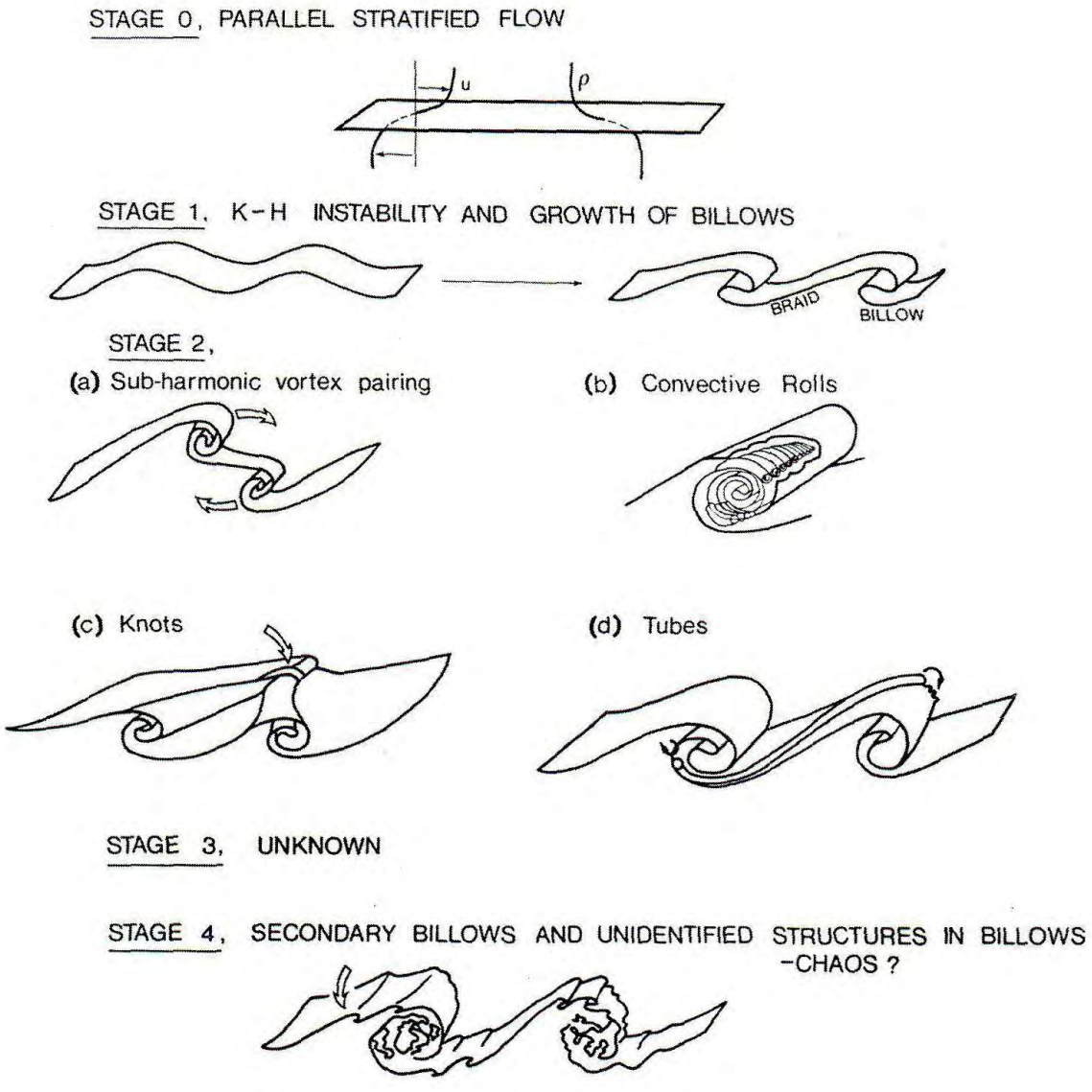

Figure 1-4: The stages in the transition from a laminar stratified shear flow to turbulence. Figure taken from Thorpe (2005)

Chapter 2.- Validations

In order to tackle the complete problem of turbulence and stratification in a channel flow, a Matlab code has been developed. The starting point is the code provided by Schmid and Henningson (2001) for laminar and non-stratified flow. Based on this, modifications have been performed to include the effects of turbulence and stratification, and also to extract more information of these flows. Each step given has been validated with the literature available. In this chapter it is described this process, as well as the main results found out through the validation. This chapter is divided into three sections. The first one is dedicated to laminar and non-stratified flow, comparisons are mainly made to Schmid and Henningson (2001). In the second section, turbulent scenario is analyzed comparing the most significant results to Del Álamo and Jiménez (2006). Finally, in the last section laminar and stratified flow is studied and the code validated with the results of the paper Biau and Bottaro (2004) among others.

2.1 Laminar and non-stratified flow

Mathematical procedures described in this section are broadly detailed in Schmid and Henningson (2001). This section, together with the Appendix, pretends to emphasize the internal structure of the code, the mathematical techniques used and its possibilities on computing flow characteristics. This is the basis from where modifications are performed in order to take on the complete problem (including both turbulent and stratified effects)

2.1.1 The velocity-vorticity formulation

The problem is governed by the Navier-Stokes and continuity equations.

$$\frac{\partial \mathbf{U}}{\partial t} + \mathbf{U}\cdot\nabla\mathbf{U} = -\nabla P + \frac{1}{\mathrm{Re}}\Delta\mathbf{U} \tag{2.1}$$

$$\nabla\cdot\mathbf{U} = 0 \tag{2.2}$$

Velocity is divided into a mean velocity and a disturbance velocity. A basic flow parallel to the x-axis that only depends on the wall-normal direction y is assumed.

$$\mathbf{U} = \overline{\mathbf{U}} + \mathbf{u} \tag{2.3}$$

$$\overline{\mathbf{U}} = (U(y),0,0) \quad \text{mean flow} \tag{2.4}$$

$$\mathbf{u} = (u,v,w) \quad \text{perturbation flow} \tag{2.5}$$

$$P = \overline{P} + p \tag{2.6}$$

where $\overline{P}$ is the mean pressure and p the perturbation pressure

When these velocity profiles are substituted into equations (1.1) and (1.2) and disturbance terms of order $O(2)$ are neglected, the linearized Navier-Stokes equations can be written:

$$\begin{aligned}
\frac{\partial u}{\partial t} + U\frac{\partial u}{\partial x} + vU' &= -\frac{\partial p}{\partial x} + \frac{1}{\mathrm{Re}}\Delta u \\
\frac{\partial v}{\partial t} + U\frac{\partial v}{\partial x} &= -\frac{\partial p}{\partial y} + \frac{1}{\mathrm{Re}}\Delta v \\
\frac{\partial w}{\partial t} + U\frac{\partial w}{\partial x} &= -\frac{\partial p}{\partial z} + \frac{1}{\mathrm{Re}}\Delta w
\end{aligned} \tag{2.7}$$

And the Continuity equation:

$$\frac{\partial u}{\partial x} + \frac{\partial v}{\partial y} + \frac{\partial w}{\partial z} = 0 \tag{2.8}$$

A prime (´) denotes y-derivative. Taking the divergence of the linearized Navier-Stokes equations (2.7) and using the continuity equation (2.8) yields an equation for the perturbation pressure.

$$\Delta p = -2U'\frac{\partial v}{\partial x} \tag{2.9}$$

When pressure is eliminated from equation (2.7b) using equation (2.9), results an equation for the wall-normal velocity v as the only variable:

$$\left[\left(\frac{\partial}{\partial t} + U\frac{\partial}{\partial x}\right)\Delta - U''\frac{\partial}{\partial x} - \frac{1}{\mathrm{Re}}\Delta^2\right]v = 0 \tag{2.10}$$

To complete the flow field problem, a second equation is needed. This is most conveniently the equation for the normal vorticity:

$$\eta = \frac{\partial u}{\partial z} - \frac{\partial w}{\partial x} \tag{2.11}$$

Combining properly the linearized momentum equation, the equation for the normal vorticity results:

$$\left[\frac{\partial}{\partial t} + U\frac{\partial}{\partial x} - \frac{1}{\mathrm{Re}}\Delta\right]\eta = -U'\frac{\partial v}{\partial z} \tag{2.12}$$

These two equation must be solved with the boundary conditions

$$v = v' = \eta = 0 \quad \text{at a solid wall (y = ±1)} \tag{2.13}$$

and the initial conditions

$$v(x, y, z, t = 0) = v_0(x, y, z) \tag{2.14}$$

$$\eta(x, y, z, t = 0) = \eta_0(x, y, z) \tag{2.15}$$

to obtain the complete description of the evolution of an arbitrary disturbance in both space and time.

2.1.2 Modal Solution. The Orr-Sommerfeld and Squire Equations

The stability of the mean flow will be analyzed with respect to wavelike velocity and pressure perturbations. Solutions are assumed to take the form

$$v(x,y,z,t) = \tilde{v}(y)\exp(i(\alpha x + \beta z - \alpha c t)) \tag{2.16}$$

$$\eta(x,y,z,t) = \tilde{\eta}(y)\exp(i(\alpha x + \beta z - \alpha c t)) \tag{2.17}$$

where $\alpha, \beta \in \Re$ are the streamwise and spanwise wave numbers and $c \in \mathbb{C}$ is the phase speed (alternatively $\omega = \alpha c$ as the frequency). The choice of a complex frequency and real wave numbers is known as the temporal problem where the spatial structure of the wavelike perturbation is unchanged and the amplitude of the wave grows or decays as time progresses (Drazin & Reid, 1981).

Introducing the modal solutions in the wall-normal velocity and normal vorticity equations are obtained

$$\left[i\alpha\left(U-c\right)\left(D^2-k^2\right) - i\alpha U'' - \frac{1}{\mathrm{Re}}\left(D^2-k^2\right)^2 \right]\tilde{v} = 0 \tag{2.18}$$

$$\left[i\alpha\left(U-c\right) - \frac{1}{\mathrm{Re}}\left(D^2-k^2\right) \right]\tilde{\eta} = -i\beta U'\tilde{v} \tag{2.19}$$

and the boundary conditions read

$$\tilde{v} = D\tilde{v} = \tilde{\eta} = 0 \tag{2.20}$$

where $D = \dfrac{d}{dy}$ denotes derivative in the inhomogeneous coordinate, and $k^2 = \alpha^2 + \beta^2$ is the spatial wave number.

Information about the components of the velocity in the streamwise and spanwise direction can be recovered easily by the expressions

$$\tilde{u} = \frac{i}{k^2}(\alpha D\tilde{v} - \beta\tilde{\eta}), \qquad \tilde{w} = \frac{i}{k^2}(\beta D\tilde{v} + \alpha\tilde{\eta}), \tag{2.21}$$

which are obtained combining properly the continuity equation and the definition of the normal vorticity

The equation for the wall-normal velocity is known as the Orr-Sommerfeld equation. It is important to notice that this equation is homogeneous.

The equation for the normal vorticity is known as the Squire equation. It is forced by the solutions of the Orr-Sommerfeld equation. This fact allows to divide the solutions into two classes. The first one is the set of Orr-Sommerfeld (OS) modes denoted as $\left\{\tilde{v}_n, \tilde{\eta}_n^p, \omega_n\right\}_{n=1}^{N}$, which have been found by solving first the Orr-Sommerfeld equation and then the Squire equation with the forcing term $\tilde{v}_n$ on the right hand. Therefore $\tilde{\eta}_n^p$ is a particular solution of the driven Squire equation. The second class of solutions is the set of Squire (SQ) modes denoted as $\left\{\tilde{v}=0, \tilde{\eta}_m, \omega_m\right\}_{m=1}^{M}$ In this case the solution to the Orr-Sommerfeld equation is identically zero, implying that the Squire equation is homogeneous.

From now on a more compact notation will be used. It is introduced the vector quantity

$$\mathbf{v} = \begin{pmatrix} \tilde{v} \\ \tilde{\eta} \end{pmatrix} \tag{2.22}$$

Orr-Sommerfeld and Squire equations are then written in the matrix form

$$-i\omega \begin{pmatrix} k^2 - D^2 & 0 \\ 0 & 1 \end{pmatrix} \begin{pmatrix} \tilde{v} \\ \tilde{\eta} \end{pmatrix} + \begin{pmatrix} \mathsf{L}_{OS} & 0 \\ i\beta U' & \mathsf{L}_{SQ} \end{pmatrix} \begin{pmatrix} \tilde{v} \\ \tilde{\eta} \end{pmatrix} = 0 \tag{2.23}$$

where $\mathsf{L}_{OS} = i\alpha U(k^2 - D^2) + i\alpha U'' + \frac{1}{\mathrm{Re}}(k^2 - D^2)^2$ (2.24)

and $\mathsf{L}_{SQ} = i\alpha U + \frac{1}{\mathrm{Re}}\left(k^2 - D^2\right)$ (2.25)

The eigenvalue problem now becomes

$$\mathbf{L}\mathbf{v} = i\omega\mathbf{M}\mathbf{v} \quad \Rightarrow \quad \mathbf{L_1}\mathbf{v} \equiv \mathbf{M}^{-1}\mathbf{L}\mathbf{v} = i\omega\mathbf{v} \tag{2.26}$$

where

$$M = \begin{pmatrix} k^2 - D^2 & 0 \\ 0 & 1 \end{pmatrix} \tag{2.27}$$

$$L = \begin{pmatrix} \mathsf{L}_{OS} & 0 \\ i\beta U' & \mathsf{L}_{SQ} \end{pmatrix} \tag{2.28}$$

2.1.3 Spectra and Eigenfunctions

The above eigenvalue problem is solved using a spectral collocation technique described in the Appendix A. The eigenvalues for the Orr-Sommerfeld equation are shown in Figure 2-1 for Re = 10000, α=1 and β=0. It is represented a set of the discrete eigenvalues, which are the less stable ones. One unstable eigenvalues is found around ω_r = 0.24, this unstable mode is expected since the critical Reynolds number for this configuration is approximately 5772. These results are in agreement with Schmid / Henningson (2001)

The eigenvalues are located on three main branches which have been labelled A ($w_r \rightarrow 0$), P ($w_r \rightarrow 1$) and S ($w_r \approx 2/3$) by Mack (1976). Typical shapes of eigenfunctions associated with three eigenvalues, one form each of the three branches are shown in Figure 2-2. It is apparent from the shape of the eigenfunctions why one usually designates the A modes as wall modes and the P modes as centre modes (Schmid & Henningson, 2001) The A modes, which have their largest variation close to the wall, have rather small phase velocities, whereas the P modes, which have their maxima close to the centre of the channel, have much higher phase speeds The S modes, which are highly damped, have a phase speed that is nearly equal to 2/3.

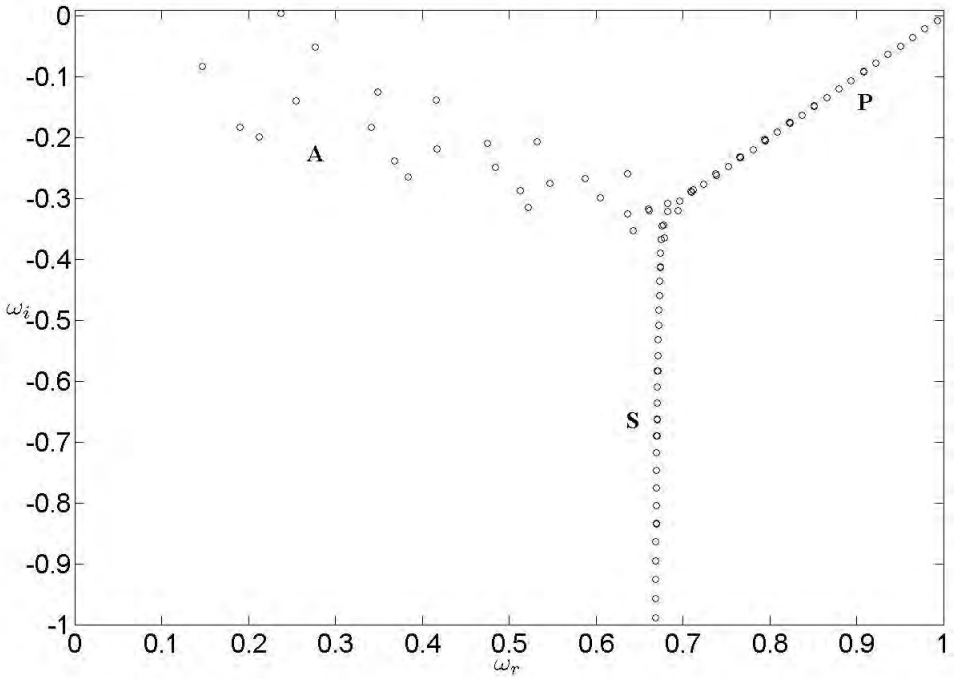

Figure 2-1: Eigenvalues for the Orr-Sommerfeld equation for Re = 10000, α=1 and β=0 in the frequency complex plane. Three branches are marked with the letters A, P and S.

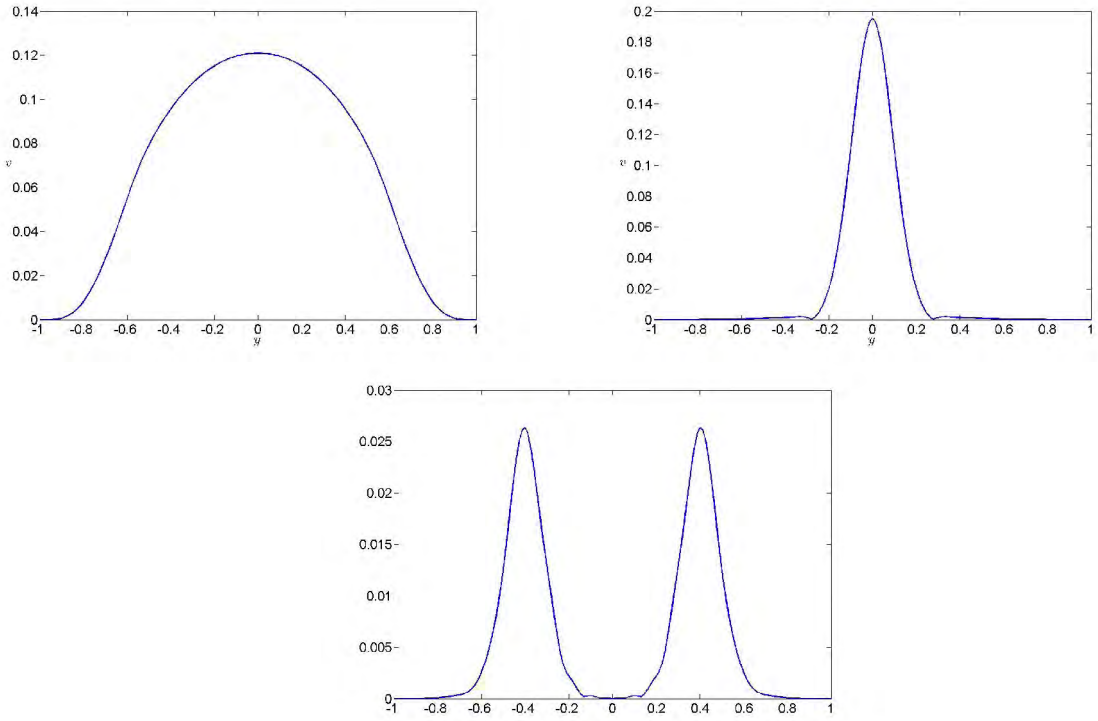

Figure 2-2: Orr-Sommerfeld eigenfunctions with Re = 5000, a =1, b = 1. Magnitude of wall-normal velocity is represented. Top left figure corresponds to A-branch, top right to P-branch and bottom to S-branch.

2.1.4 Neutral curve

The curve that defines the boundary between areas in parameter space where exponentially growing solutions exist and where they do not, is called the neutral curve. Thus, it represents the frontier between stable and unstable solutions of the Orr-Sommerfeld equation. In the present result it has been computed in the (α,Re) plane by selecting the points where the imaginary part of the least damped eigenvalue is zero.

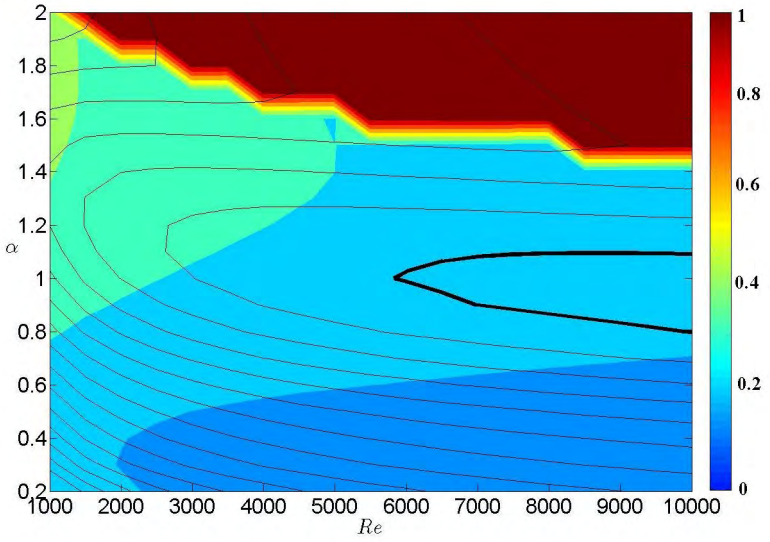

Figure 2-3: Neutral curve for the laminar and non-stratified channel flow. Neutral curve corresponds to the black thick line. The rest of the lines are the contours of constant growth rate, c_i, with levels -0.01(-0.01)-0.14. Coloured levels are contours of constant phase velocity c_r of the least stable eigenmode.

In Figure 2-3 can be noted that for the unstable waves the phase speed is about 20 to 25 percent of the centreline velocity. At the top of that figure a discontinuity in the phase speed is observed, this signifies a change of the least stable eigenmode from a wall mode of the A branch at the lower end of the figure to a centre mode on the P branch in the upper part of the figure. It can be also seen that the lower Reynolds number at which an unstable eigenvalue is found is around Re=5772 (Orszag, 1991).

The results obtained in this section (neutral curve, phase speed and growth rate of the perturbation in the (α,Re) plane) have good agreement with Schmid & Henningson (2001).

2.1.5 Transient growth.

Solutions of the form

$$v(x,y,z,t) = \tilde{v}(y,t)\exp(i\alpha x + i\beta z) \quad (2.29)$$

$$\eta(x,y,z,t) = \tilde{\eta}(y,t)\exp(i\alpha x + i\beta z) \quad (2.30)$$

are assumed for the Initial Value Problem taken into account the homogeneous nature of the streamwise and spanwise coordinate directions.

Following the same path as below to derive the disturbance equations, and using a matrix form with the vector variable

$$\mathbf{v} = \begin{Bmatrix} \tilde{v} \\ \tilde{\eta} \end{Bmatrix} \tag{2.31}$$

the linear initial value problem can be written as

$$\mathbf{M}\frac{\partial \mathbf{v}}{\partial t} = \mathbf{L}\mathbf{v} \qquad \Rightarrow \qquad \frac{\partial \mathbf{v}}{\partial t} = \mathbf{M}^{-1}\mathbf{L}\mathbf{v} = \mathbf{L}_1\mathbf{v} \tag{2.32}$$

The formal solution of this problem is as follows

$$\mathbf{v} = \mathbf{v}(y, t=0)\exp(i\mathbf{L}_1 t) \tag{2.33}$$

The initial value problem can be restated into a simpler form, if the vector variable $\mathbf{v}$ is expanded into the basis $\{\hat{\mathbf{q}}_1, \hat{\mathbf{q}}_2, ..., \hat{\mathbf{q}}_n\}$ formed by the N eigenfunctions of $\mathbf{L}_1$. These eigenfunctions have been normalized to unitary energy norm $\|\hat{\mathbf{q}}\|_E^2 = 1$ (as explained in Appendix A)

$$\mathbf{v}(y,t) = \sum_{n=1}^{N} \kappa_n(t)\hat{q}_n(y) \tag{2.34}$$

Substituting this expression into the linear initial value problem yields to the equation

$$\frac{d\boldsymbol{\kappa}}{dt} = i\boldsymbol{\Lambda}\boldsymbol{\kappa} \tag{2.35}$$

whose formal solution can be written as

$$\boldsymbol{\kappa} = \boldsymbol{\kappa}(t=0)\exp(-i\boldsymbol{\Lambda}t) = \boldsymbol{\kappa}_0\exp(-i\boldsymbol{\Lambda}t) \tag{2.36}$$

where $\boldsymbol{\Lambda}$ is the diagonal matrix of the eigenvalues of $\mathbf{L}_1$

$$\Lambda = diag\{\omega_1, \omega_2, ..., \omega_N\} \tag{2.37}$$

and

$$\boldsymbol{\kappa} = (\boldsymbol{\kappa}_1, \boldsymbol{\kappa}_2, ..., \boldsymbol{\kappa}_N) \tag{2.38}$$

Even when the solution of the problem is stable, that is to say, when the imaginary part of the frequency or the phase speed is less than zero (Imag(ω)<0), perturbations on the velocity or the pressure can grow initially. This phenomena is due to the non-orthogonality of the eigenfunctions $\hat{\mathbf{q}}$. It can occur that in a stable case a perturbation $\mathbf{v}$, which is a combination of several eigenfunctions, grow initially because of the different rates of decaying of each eigenfunction.

The purpose of the next study is to search for initial disturbances that maximize short-term growth. The maximum possible amplification G of initial energy density is defined as

$$G(t) = \max \frac{\left\| \tilde{\mathbf{v}}(y,t) \right\|_E^2}{\left\| \tilde{\mathbf{v}}(y,0) \right\|_E^2} \tag{2.39}$$

To develop this expression, it is necessary to see before the inner product of the eigenfunctions in the energy norm.

$$\left\| \hat{\mathbf{q}}_i, \hat{\mathbf{q}}_j \right\|_E^2 = A_{ij} \tag{2.40}$$

where A is both an Hermitian and positive definite matrix, therefore it can be factored according to $\mathbf{A} = \mathbf{F}^{\mathbf{H}}\mathbf{F} = \left\| \hat{\mathbf{q}}, \hat{\mathbf{q}} \right\|_E^2$

The energy norm of any perturbation can be written as

$$\left\| \tilde{\mathbf{v}} \right\|_E^2 \equiv \left\| \tilde{\mathbf{v}}, \tilde{\mathbf{v}} \right\|_E^2 = \left\| \boldsymbol{\kappa}\hat{\mathbf{q}}, \boldsymbol{\kappa}\hat{\mathbf{q}} \right\|_E^2 = \boldsymbol{\kappa}^{\mathbf{H}}\mathbf{F}^{\mathbf{H}}\mathbf{F}\boldsymbol{\kappa} = \left\| \mathbf{F}\boldsymbol{\kappa} \right\|_2^2 \tag{2.41}$$

Thus, the maximum possible amplification

$$G(t) = \max \frac{\left\| \tilde{\mathbf{v}}(y,t) \right\|_E^2}{\left\| \tilde{\mathbf{v}}(y,0) \right\|_E^2} = \frac{\left\| \mathbf{F}\boldsymbol{\kappa}(t) \right\|_2^2}{\left\| \mathbf{F}\boldsymbol{\kappa}(0) \right\|_2^2} = \frac{\left\| \mathbf{F}\exp(-i\boldsymbol{\Lambda}t)\boldsymbol{\kappa}(0) \right\|_2^2}{\left\| \mathbf{F}\boldsymbol{\kappa}(0) \right\|_2^2} \tag{2.42}$$

Changing the basis of the coefficients $\boldsymbol{\kappa}(0)$ in the way $\boldsymbol{\phi} = \mathbf{F}\boldsymbol{\kappa}(0)$, the above expression can be simplified

$$G(t) = \max \frac{\left\| \tilde{\mathbf{v}}(y,t) \right\|_E^2}{\left\| \tilde{\mathbf{v}}(y,0) \right\|_E^2} = \ldots = \frac{\left\| \mathbf{F}\exp(-i\boldsymbol{\Lambda}t)\boldsymbol{\kappa}(0) \right\|_2^2}{\left\| \mathbf{F}\boldsymbol{\kappa}(0) \right\|_2^2} = \frac{\left\| \mathbf{F}\exp(-i\boldsymbol{\Lambda}t)\mathbf{F}^{-1}\boldsymbol{\phi} \right\|_2^2}{\left\| \boldsymbol{\phi} \right\|_2^2} = \left\| \mathbf{F}\exp(-i\boldsymbol{\Lambda}t)\mathbf{F}^{-1} \right\|_2^2 = \sigma_1^2 \tag{2.43}$$

where σ_1 is the principal singular value of the matrix $\mathbf{F}\exp(-i\boldsymbol{\Lambda}t)\mathbf{F}^{-1}$ decomposed in SVD.

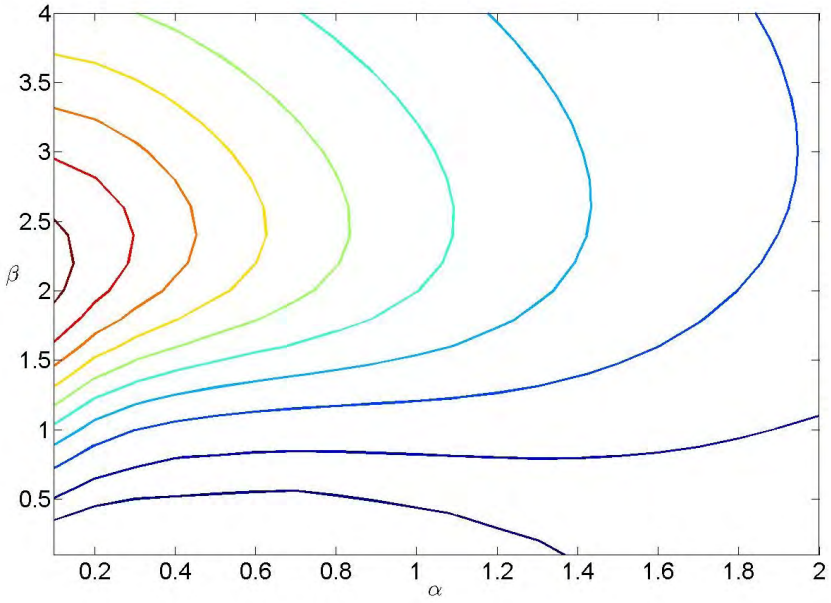

Figure 2-4: Contours of Gmax with Re = 1000. The curves from blue to red correspond to Gmax = 10, 20, 40, ..., 140, 160, 180.

Using these procedures the maximum energy amplification, G, for the laminar flow has been computed in the (α, β) plane at Re=1000. The range of wave numbers in the streamwise direction has been selected of $\alpha \in [0.1 \quad 2]$, and in the spanwise direction of $\beta \in [0 \quad 4]$. At this Reynolds number, as the neutral curve computed in the preceding section shows, linear stability predicts a stable flow. However, it can be seen in Figure 2-4 how the energy of the most amplified perturbation grows by a factor of O(180). Figure 2.-4 has a perfect agreement with Schmid & Henningson (2001)

The initial condition that will reach the maximum possible amplification can be determined after having used the singular value decomposition (SVD). This initial condition is denoted by $\mathbf{v}_0$. The energy of the initial condition will have grown by a factor of $\left\| \mathbf{F} \exp(-i\boldsymbol{\Lambda} t_{\max}) \mathbf{F}^{-1} \right\|$ at a later time t_{max} because it has been chosen to be the optimal perturbation at this specific time. We therefore has the equation

$$\mathbf{B}\boldsymbol{\phi}(0) = \mu \boldsymbol{\phi}(t_{\max}) \tag{2.44}$$

where

$$\mathbf{B} = \mathbf{F} \exp(-i\boldsymbol{\Lambda} t_{\max}) \mathbf{F}^{-1} \qquad \textit{and} \qquad \mu = \left\| \mathbf{B} \right\|_2 = \sigma_1 \tag{2.45}$$

As μ is equal to the principal singular value, the search of the optimal initial condition $\mathbf{v}_0$ can be solved by decomposing the matrix B into the Singular Value Decomposition (SVD)

$$\mathbf{B} = \mathbf{U}^{\mathbf{T}} \mathbf{S} \mathbf{V} \qquad \Rightarrow \qquad \mathbf{B}\mathbf{U} = \mathbf{S}\mathbf{V} \tag{2.46}$$

Concentrating only in the first column of U and V, which corresponds to the principal singular value

$$\mathbf{B}\mathbf{u}_1 = \sigma_1 \mathbf{v}_1 \tag{2.47}$$

Therefore

$$\mathbf{u}_1 = \boldsymbol{\phi}_1 \tag{2.48}$$

Undoing the two basis change, the initial perturbation $\mathbf{v}_0$ can be recovered.

$$\mathbf{k}(0) = \mathbf{F}^{-1} \boldsymbol{\phi} \qquad \Rightarrow \qquad \mathbf{v}_0 = \left[\hat{\mathbf{q}} \right] \mathbf{F}^{-1} \boldsymbol{\phi} \tag{2.49}$$

2.2 Turbulent and non-stratified case.

2.2.1 Governing equations

The linearized dynamics of small-amplitude perturbations to the mean profile U(y) in a turbulent channel are governed by

$$\partial_t \mathbf{u} + U\partial_x \mathbf{u} + (vU',0,0) = -\nabla p + \left[\upsilon_t\left(\partial_{xx}+\partial_{zz}\right) + \partial_y\left(\upsilon_t\partial_y\right)\right]\mathbf{u} \qquad (2.50)$$

this equation differs from the linearized Navier-Stokes equation in the viscous terms, where the constant molecular viscosity is substituted by a variable turbulent eddy viscosity $\upsilon_t(y)$ to model the interaction of the perturbations with the background turbulence.

It is used the Cess (1958) analytic approximation for the turbulent eddy viscosity,

$$\upsilon_t = \upsilon\left\{\frac{1}{2}\left[1+\frac{1}{9}K^2\,\mathrm{Re}_\tau^2\left(2y-y^2\right)^2\left(3-4y+2y^2\right)^2\left(1-\exp\left(-\frac{y\,\mathrm{Re}_\tau}{A}\right)\right)^2\right]^{\frac{1}{2}}+\frac{1}{2}\right\} \qquad (2.51)$$

where the dimensionless coordinate y and the molecular viscosity υ are included. This expression has been used in several studies such as Reynolds & Tiederman (1967) , Reynolds & Hussain (1972) and Del Álamo & Jiménez (2006). One parameter of the Cess formula is the friction Reynolds number, that characterizes turbulent flow, and is defined by $\mathrm{Re}_\tau \equiv \frac{u_\tau h}{\upsilon} = \frac{h}{\delta_v}$, where u_τ is the friction velocity and $\delta_v \equiv \upsilon\sqrt{\rho/\tau_w} = \upsilon/u_\tau$ is the viscous lengthscale. Apart from the Reynolds number, the Cess formula has two parameters that have to be fixed. In this work, these parameters have been taken as K=0.426 and A=25.4, which are recommended by Del Álamo & Jiménez (2006). They have been kept constant for all the Reynolds number explored in this study. There are other proposals for the values of these parameters, as the ones used by Reynolds & Hussain (1972), K = 0.426 and A = 29, which are reasonably similar. The corresponding eddy viscosities are represented in Figure 2-5. They scale in wall units near the wall and follow the similarity law $\upsilon_\tau^+ = \kappa y^+$ in the logarithmic layer. The mean velocity profile is given by integrating (2.51). Velocity profiles for a range of Reynolds number are represented in Figure 2-5, where it is shown that they follow the log law $u^+ = (1/\kappa)\ln y^+ + B$ in the logarithmic layer (with parameters set to κ=0.41 and B=5.2).

The mean velocity profile can be obtained from the mean Navier-Stokes equation in the streamwise direction:

$$0 = -\frac{\partial p}{\partial x} + \frac{\partial}{\partial y}\left(\upsilon_t\frac{\partial U}{\partial y}\right) \qquad (2.52)$$

and fixing $\partial p/\partial x = 1$, then the mean velocity profile is given by integrating $(1-y)/\upsilon_t$, where y is the non-dimensional coordinate in the vertical direction.

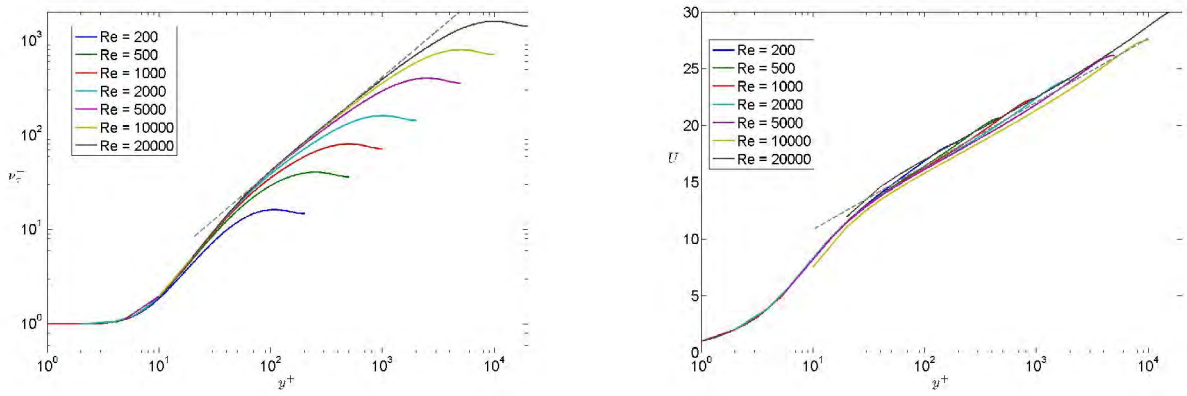

Figure 2-5: Left plot shows eddy viscosity profiles of Cess formula (1958) at different Reynolds numbers, whereas right plot shows mean velocity profiles at the same range of Reynolds numbers.

The mathematical procedure to achieve a similar velocity-vorticity formulation as in the laminar and non-stratified case is analogous. New terms in equations appear due to the dependence of the eddy viscosity with the wall-normal direction. Thus, the laplacian of the pressure takes the form,

$$\Delta p = -2U'\partial_x v + \left[\upsilon_t'\left(\partial_{xx} + \partial_{zz}\right) + \partial_y\left(\upsilon_t'\partial_y\right)\right]v \tag{2.53}$$

where the differences in comparison with the first validation come from the derivatives of the eddy viscosity.

In order to eliminate the pressure in the equations to be solved, the laplacian of the momentum equation in the wall-normal direction is taken, and substituted the expression (2.50). In this way it is reached an equation with the wall-normal velocity v as the only variable.

$$\left[\left(\partial_t + U\partial_x\right)\Delta - U''\partial_x - \upsilon_t\Delta^2 - \left(2\upsilon_t'\partial_y\right)\Delta - \upsilon_t''\partial_{yy}\right]v = 0 \tag{2.54}$$

The second equation needed to complete the problem is the normal vorticity equation. Combining properly the linearized momentum equation in the streamwise and spanwise directions, the equation for the normal vorticity results

$$\left[\partial_t + U\partial_x - \upsilon_t\Delta - \upsilon_t'\partial_y\right]\eta = -U'\partial_z v \tag{2.55}$$

Making use of the Chebyshev expansion and considering the same modal solution as in the laminar and non-stratified case, equations (2.54) and (2.55) take the following form:

$$\left[\left(U-c\right)\left(D^2-k^2\right) - U'' - \frac{\upsilon_t}{i\alpha}\left(D^2-k^2\right)^2 - \frac{1}{i\alpha}\left(\upsilon_t''D^2 + 2\upsilon_t'D^3 - 2k^2\upsilon_t'D\right)\right]\tilde{v} = 0 \tag{2.56}$$

$$\left[i\alpha\left(U-c\right) - \upsilon_t\left(D^2-k^2\right) - \upsilon_t'D\right]\tilde{\eta} = -i\beta U'\tilde{v} \tag{2.57}$$

Because of the wide range of Reynolds number studied in this section, the number of grid points used in the computation of each case plays a fundamental role. Table 2-1

shows the numerical resolution for each Reynolds number, which is enough to resolve the eigenfunctions for the smallest waves considered at each concrete case (Del Álamo & Jiménez, 2006)

Re_τ	200	500	1000	2000	5000	10000	20000
Grid points	130	180	250	320	400	480	514

Table 2-1: Numerical resolution used for each Reynolds number.

2.2.2 Transient Growth

The maximum amplification is computed by applying the same procedures detailed in §1.5. As it was noted above, this method also produces the most amplified solutions and the optimal initial conditions. Figure 2-6[2] displays the maximum energy growth that can reach a perturbation of size λ_x/h and λ_z/h in the streamwise and spanwise direction respectively. This figure indicates that there is transient energy growth for $\lambda_x \geq \lambda_z$, consistent with the streamwise-elongated structures commonly observed in turbulent channels. For each value of λ_z, the maximum energy amplification initially grows with the streamwise wavelength but becomes constant for very long perturbations. These results fit well with Del Álamo and Jiménez (2006). For simplicity, this range of asymptotic λ_x independence will be focused on.

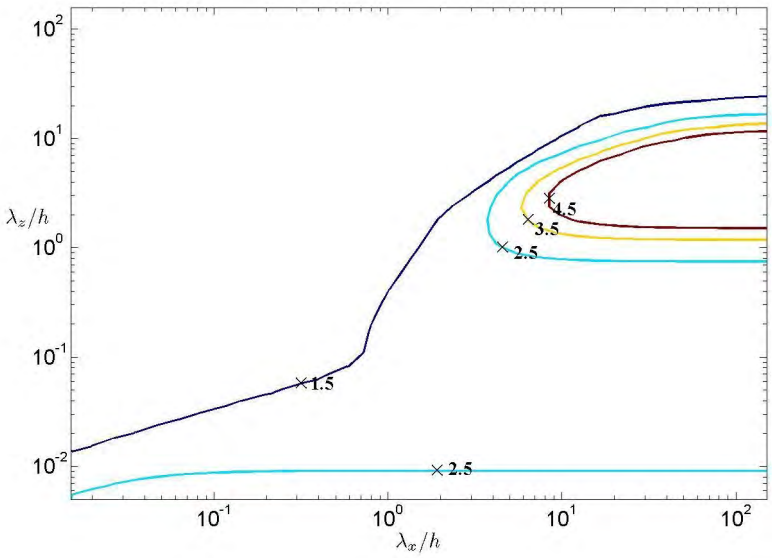

Figure 2-6: Maximum transient growth G for $Re=2x10^4$ as a function of λ_x/h and of λ_z/h

The most amplified solutions reproduce the organization of turbulent structures in actual channels. In fact, since turbulence acts as a continuous source of random disturbances of all sizes, the regions of high amplification should be associated with prevalent structures in the flow. This is explored in Figures 2-7 and 2-8 by displaying G as a function of λ_z for different Reynolds numbers. In all cases $\lambda_x=60h$.

[2] λ_x and λ_z are the wave length of the perturbations. They are defined from the wave number α and β as follows: $\lambda_x=2\pi/\alpha$ and $\lambda_z=2\pi/\beta$

Figure 2-7 shows that expressing the widths in wall units collapses the positions of the small-scale peaks of G around $\lambda_z^+ = 100$. This agrees remarkably well with the width of the near wall streaks (Smith & Metzler 1983). The same is true for large global structures documented by Del Álamo & Jiménez (2003) and Del Álamo et al. (2004). They have widths of the order of $\lambda_z = 3h$, similar to the common position of the large-scale peaks of G in Figure 2-8

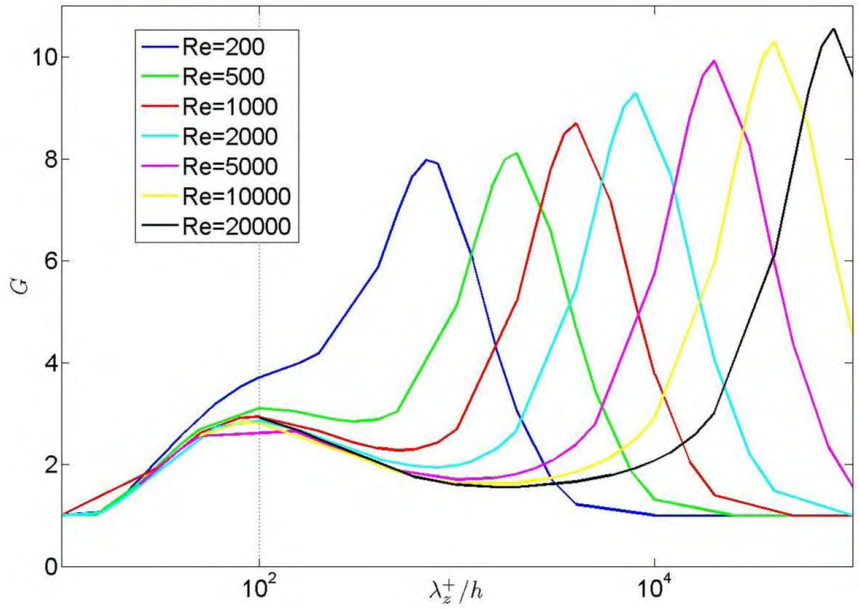

Figure 2-7: Maximum energy amplification G(60h,λ_z) for different Reynolds numbers, represented as a function of the wavelength in the spanwise direction expressed in wall units. The vertical line is $\lambda_z^+ = 100$.

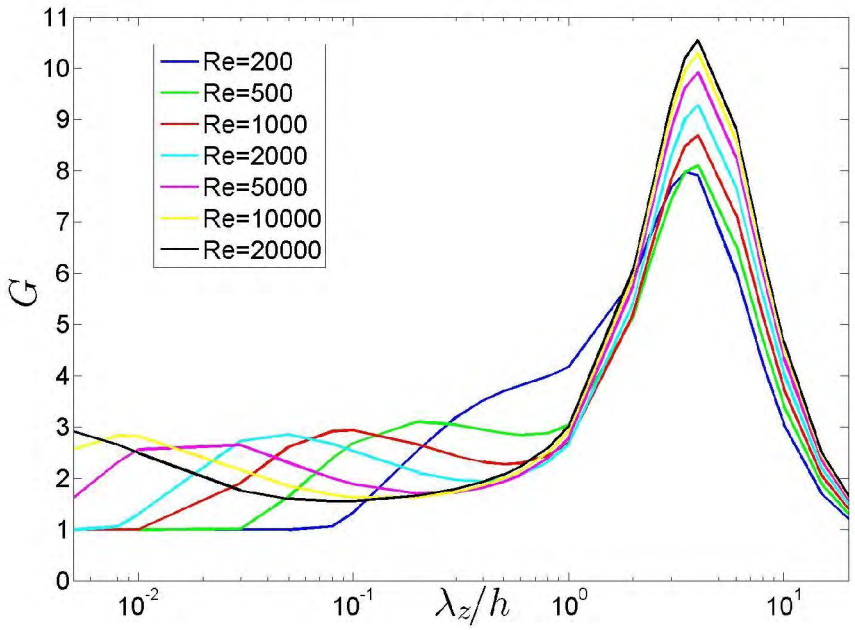

Figure 2-8: Maximum energy amplification G(60h,λ_z) for different Reynolds numbers, represented as a function of the wavelength in the spanwise direction.

Results presented here differ from Del Álamo and Jiménez (2006) in the maximum energy amplification, G_{max}, reached in large-scale structures. This difference is due to the terms in the derivative of the viscosity that were neglected by Del Álamo and Jiménez (2006) in the equation of the laplacian of the pressure. In that work, the large scale maximum remains in the same position but its value decreases as the Reynolds number increases (from G≈8 at Re=200 to G≈5.5 at Re=20000). By contrast, in this study the value of the maximum energy amplification for the large-scale structures increases with the Reynolds number as Figure 2-8 shows. This agrees with the analysis by Jiménez (2007) where a Reynolds-number dependence of u'^{+} is observed. It should be remarked that in the optimal time for the maximum energy amplification almost all the kinetic energy is contained in the streamwise motions (see Figure 2-9)[3]. Thus, a Reynolds number dependence of u'^{+} is equivalent to a Reynolds number dependence of G. In Figure 2-10 it is shown that the dependence disappears (lines collapse) when the spectral energy associated with the global motions is removed. That would imply that the large-scale modes are directly dependent to the Reynolds number and are responsible of a growth in energy with Re, as the model of this study predicts.

The tendency the maximum G at different Reynolds numbers fits a logarithmic law of Re in the way $\max(G_{\max}) = 0.6315\log(\mathrm{Re}_\tau) + 4.413$ (see Figure 2-11).

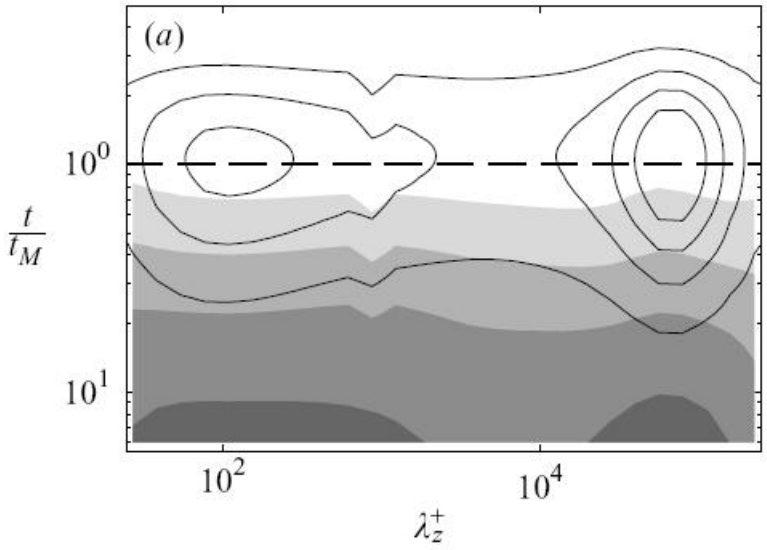

Figure 2-9: Component-wise energy amplification as a function of λ_z^+ and t/t_M; λ_x=60h; Re_τ=2x10^4; the line contours come from the streamwise component, G_u, and the levels represented are 1(+1)4; the shaded contours come from the transverse component, G_{vw}, and the levels represented are 0.2(+0.2)0.8. Figure taken from Del Álamo and Jiménez (2006)

[3] Figure 2-9 (taken from Del Álamo and Jiménez, 2006) displays the component-wise energy amplification as a function of the spanwise wave length in wall units, λ_z^+, and the time scaled with the optimal time, for λ_x=60h and Re_τ=2x10^4. It can be noticed how, initially, almost all the kinetic energy is contained in the transverse motions. These motions decay with time under the effect of eddy viscosity generating streamwise velocity fluctuations. At optimal time, kinetic energy reaches its maximum and it is essentially composed by the streamwise motions.

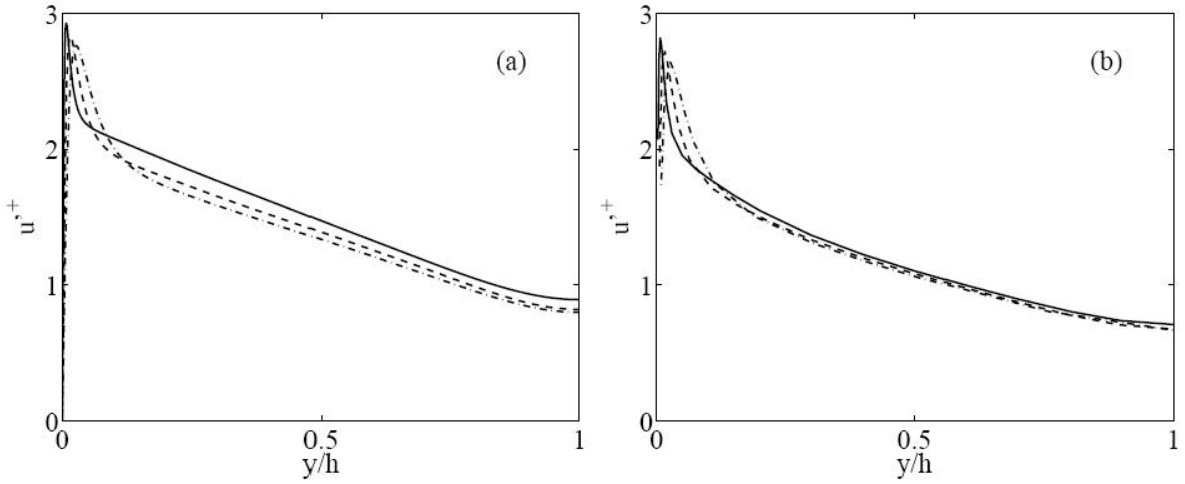

Figure 2-10: Root mean-square intensity of the fluctuations of the streamwise velocity in channels at Reynolds number –.– 547; - - - 934; ——2003 (a) Full velocity fluctuations. (b) With the energy removed for structures longer than $\lambda_x=6h$, and wider than $\lambda_z=h$. Figure taken from Jiménez (2007)

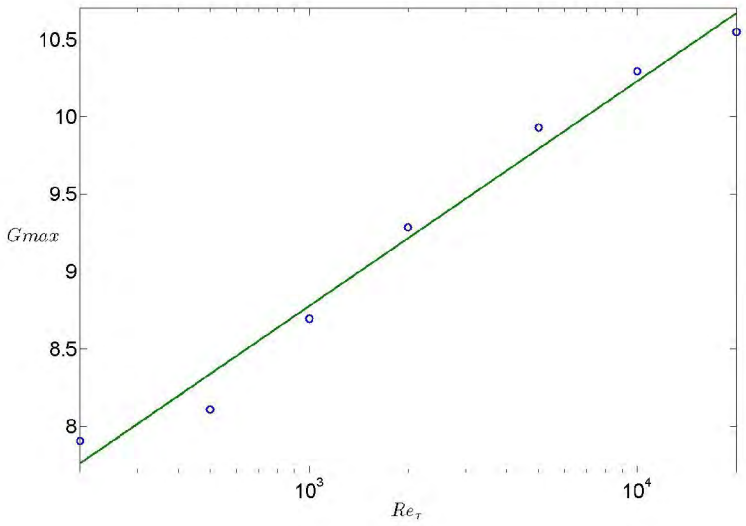

Figure 2-11: Maximum value of G_{max} in function of the friction Reynolds number. Blue circular marks corresponds to the results of the linear model, and the green line to the law $\max(G_{max})=0.6315 \log(Re_\tau) + 4.413$

2.3 Stratified laminar case

2.3.1 Governing equations.

Poiseuille flow between two horizontal planes is again considered. The buoyancy force is induced by a density distribution, which has a weak gradient. Therefore, fluid properties are assumed to be constant, and a thermal distribution could be considered instead of the density one since both are proportional. Geometry is the same as in former cases, and the planes of the channel are perpendicular to the acting gravity, as well as to the mean density profile, which takes in this way the dimensionless simple form:

$$\overline{\rho}(y) = \frac{1-y}{2} \tag{2.58}$$

The linearized disturbance equations[4] which govern the stability of a stratified parallel shear flow are derived with the usual Boussinesq approximation, i.e. neglecting variations in density except where they are multiplied by the gravitational acceleration[5]. A new term appears with respect to the non-stratified case, and it is related to the gravity force acting through the density distribution. When non-dimensionalizing the equations another parameter, apart from the Reynolds number, have influence in the behaviour of the flow. It is the Richardson number, defined as follows:

$$Ri = \frac{g\,h\,\Delta\rho}{U_c^2\,\rho_0} \tag{2.59}$$

where g is the usual gravitational acceleration constant and ρ_0 is the characteristic density of the fluid. Thus, the vectorial form of the momentum equation reads

$$\partial_t \mathbf{U} + \mathbf{U}\cdot\nabla\mathbf{U} = -\nabla P + \frac{1}{\mathrm{Re}}\Delta\mathbf{U} - \mathrm{Ri}\rho\mathbf{j} \tag{2.60}$$

where $\mathbf{j}$ is the unitary vector in the vertical direction.

Although there is a density gradient in the wall-normal direction, flow is still considered incompressible. Therefore, continuity equation remains as the divergence of the velocity vector $\nabla\cdot\mathbf{U} = 0$. With these two equations and the definition of vorticity can be derived easily the equivalent Orr-Sommerfeld and Squire equations for the stratified case. However, there is another variable, the perturbation density ρ, that stays undetermined. That is to say, another equation is needed to have a closed problem. The set of equations are complete in this way by the energy equation that written in a dimensionless form is:

---

[4] The notation here used for the density is the following:
S= $\overline{\rho}$ +ρ, where S is the total density, $\overline{\rho}$ is the mean density profile and ρ is the density perturbations. These quantities are already normalized by the characteristic density of the fluid ρ_0.

[5] The basis of this approximation is that there are flows in which the temperature varies little, and therefore the density varies little, yet in which the buoyancy drives the motion. Then the variation of density is neglected everywhere except in the buoyancy (Drazin & Reid, 1981)

$$\frac{\partial S}{\partial t} + \mathbf{U}\cdot\nabla S = \frac{1}{\mathrm{Re}\,\mathrm{Pr}}\Delta S \tag{2.61}$$

where Pr is the Prandtl number.

The mathematical procedure to achieve a similar velocity-vorticity formulation as in the former cases is analogous. Taking the divergence of the momentum equation, an expression of the laplacian is reached

$$\Delta p = -\left(2U'\partial_x v + \mathrm{Ri}\,\rho'\right) \tag{2.62}$$

which allows to eliminate the pressure component in the linearized Navier-Stokes equation in the wall-normal direction. Afterwards, combining properly the streamwise and spanwise momentum equations, an equation for the vorticity is obtained. After some algebraic work, the set of equations to be solved reads:

$$\begin{aligned}
&\left[\left(\partial_t + U\partial_x\right)\Delta - U''\partial_x - \frac{1}{\mathrm{Re}}\Delta^2\right]v = -\mathrm{Ri}\left(\partial_{xx} + \partial_{zz}\right)\rho \\
&\left[\left(\partial_t + U\partial_x\right) - \frac{1}{\mathrm{Re}}\Delta\right]\eta = -U'\partial_z v \\
&\left[\left(\partial_t + U\partial_x\right) - \frac{1}{\mathrm{Pr}\,\mathrm{Re}}\Delta\right]\rho = -\overline{\rho}'\,v
\end{aligned} \tag{2.63}$$

where $\overline{\rho}' = d\overline{\rho}/dy = -1/2$. The boundary conditions are $v = \partial v/\partial y = \eta = \rho = 0$ at both walls.

Making use of the Chebyshev expansion and considering the same modal solution as in the laminar and non-stratified case, the set of equations (2.63) takes the following form:

$$\begin{aligned}
&\left[i\alpha\left(U-c\right)\left(D^2-k^2\right) - i\alpha U'' - \frac{1}{\mathrm{Re}}\left(D^2-k^2\right)^2\right]\tilde{v} - \mathrm{Ri}\,k^2\tilde{\rho} = 0 \\
&\left[i\alpha\left(U-c\right) - \frac{1}{\mathrm{Re}}\left(D^2-k^2\right)\right]\tilde{\eta} - i\,\beta U'\tilde{v} = 0 \\
&\left[i\alpha\left(U-c\right) - \frac{1}{\mathrm{Pr}\,\mathrm{Re}}\left(D^2-k^2\right)\right]\tilde{\rho} + \overline{\rho}'\,\tilde{v} = 0
\end{aligned} \tag{2.64}$$

It is convenient to notice that the procedures to compute the maximum energy amplification, G, slightly differs in the stratified flow respect to the unstratified one. The difference lie in the way the eigenfunctions are normalized with the energy norm, since in the stratified case potential energy must be also taken into account. Considerations made to include the term of potential energy into the normalization are fully described in section 5 of the Appendix.

2.3.2 Comparison with previous work

In order to prove the validity of the code developed to laminar and stratified plane Poiseuille flow, results from Gage and Reid (1968) and Biau and Bottaro (2004) have been compared to the ones achieved. Good agreement is found, as Table 2-2 shows.

Ri	Gage and Reid			Biau and Bottaro			Present results		
	Re_c	α_c	c_c	Re_c	α_c	c_c	Re_c	α_c	c_c
0	5396	1.022	0.2672	5772.2	1.020	0.2639	5772.2	1.020	0.2639
0.0304	7133	1.005	0.2482	7600.6	10.031	0.2452	7600.6	10.031	0.2452
0.0616	9718	0.998	0.2285	10246	0.9845	0.2261	10246	0.9845	0.2261
0.0952	13755	0.964	0.2075	14451.5	0.9637	0.2057	14451.5	0.9637	0.2057

Table 2-2: Neutral stability results for various Ri values.

2.3.3 Neutral curve and transient growth.

The neutral curve for the configuration has been computed in the (Re, Ri) plane. A range of wave numbers α have been explored (from α = 0.990 to α = 1.020, each 0.0025) in order to determine the neutral curve, that is to say, the points in the (Re,Ri) plane in which for a lower Reynolds number, instability can occur. This range of α has been chosen attending to the results shown in Table 2-1. A zero value of β and Pr = 0.7 have been used.

Neutral curve in this study is then compared to the one computed by Biau and Bottaro (2004), finding good agreement between both.

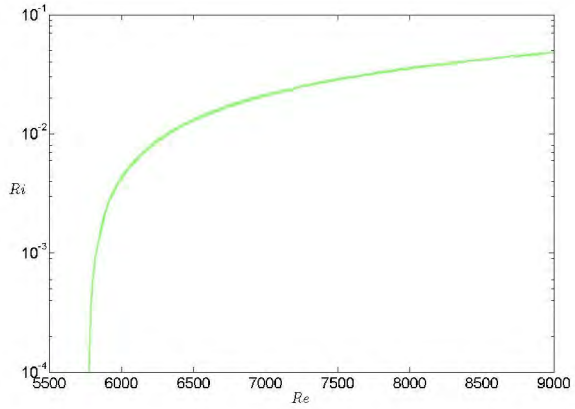

Figure 2-12: Neutral curve in the (Re, Ri) plane for Pr = 0.7. Area at the left of the curve indicates the linearly stable region.

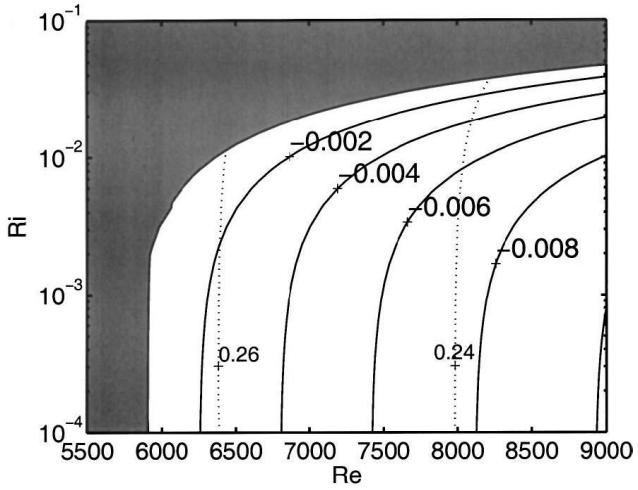

Figure 2-13: Contours of growth rate α_i (continuous lines), and corresponding angular frequency of largest growth ω (dotted lines) in the (Re, Ri) plane for Pr=0.7. Figure taken from Biau and Bottaro (2004)

It can be observed that the value of growth rate decreases for increasing Richardson numbers; Gage and Reid (1968) had already shown such a trend, and demonstrated that the flow becomes completely stabilized for Ri>0.443. As can be seen buoyancy strongly influences the critical value of the Reynolds number.

Computations with different Prandtl number have been made obtaining similar results as in Figure 2-12. This fact states the weak influence of the Prandtl number in this study, which agrees with Biau and Bottaro (2004).

The influence of the Richardson number can be observed in the contours of maximum energy amplification in the α-β plane for eight cases at different Ri numbers (from $Ri=1x10^{-4}$ to $2x10^{-2}$), which are presented below. As it could be deduced from the fact of having stably stratification, the main effect of an increasing Ri number is the drop in energy of the transient growth, that is to say, it has a stabilizing effect. The other point to highlight is the movement of the maximum from $\alpha=0$ (for $Ri=1x10^{-4}$) to $\alpha=0.8$ ($Ri=2x10^{-2}$) remaining in the same β-band of around 2.5. That means that the most-amplified structures (the ones that could lead to turbulence) vary their sizes from structures that occupy the whole channel in the x-direction with a width of $\lambda_z=2.6$, to others smaller of $\lambda_x=8$ and $\lambda_z=2.8$ as the Ri number increases.

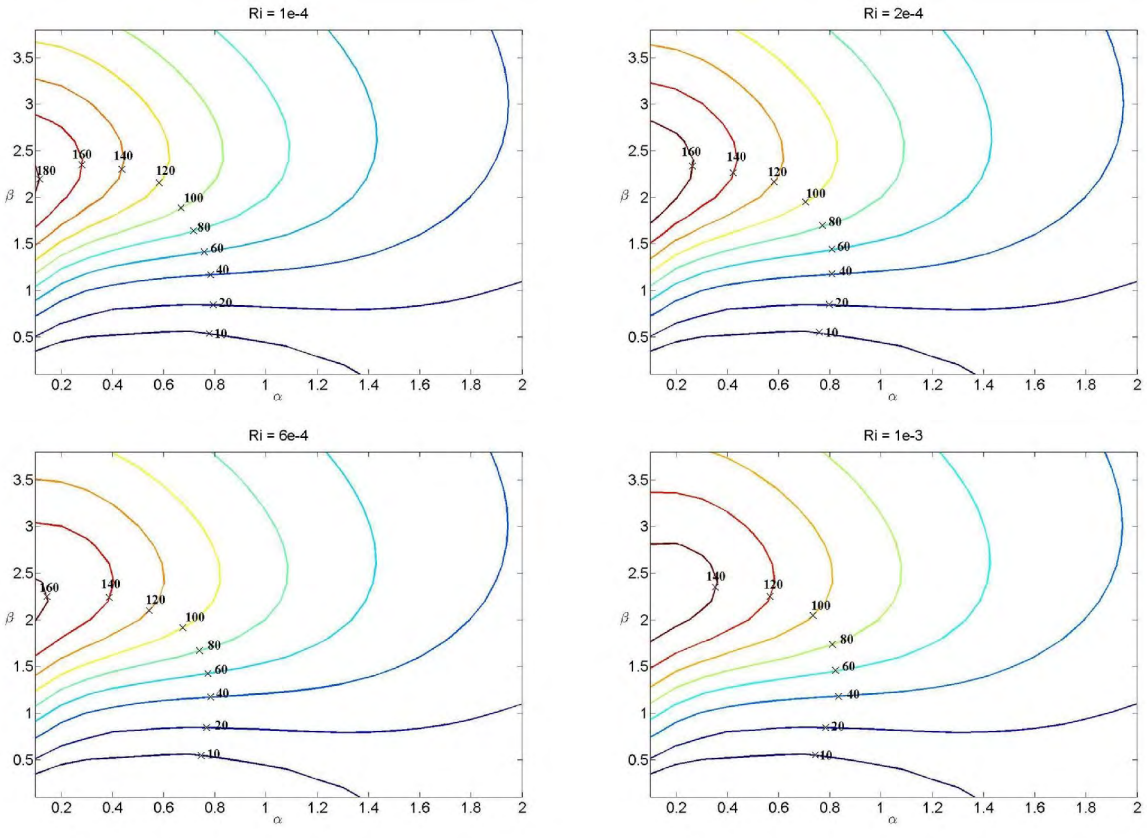

Figure 2-14: Contours of maximum energy amplification in the (α,β) plane for a laminar and stratified channel flow at Re=1000. Four cases at a different Richardson number are presented: top left figure, $Ri=1\cdot10^{-4}$; top right figure, $Ri=2\cdot10^{-4}$; bottom left figure $Ri=6\cdot10^{-4}$; and bottom right figure, $1\cdot10^{-3}$

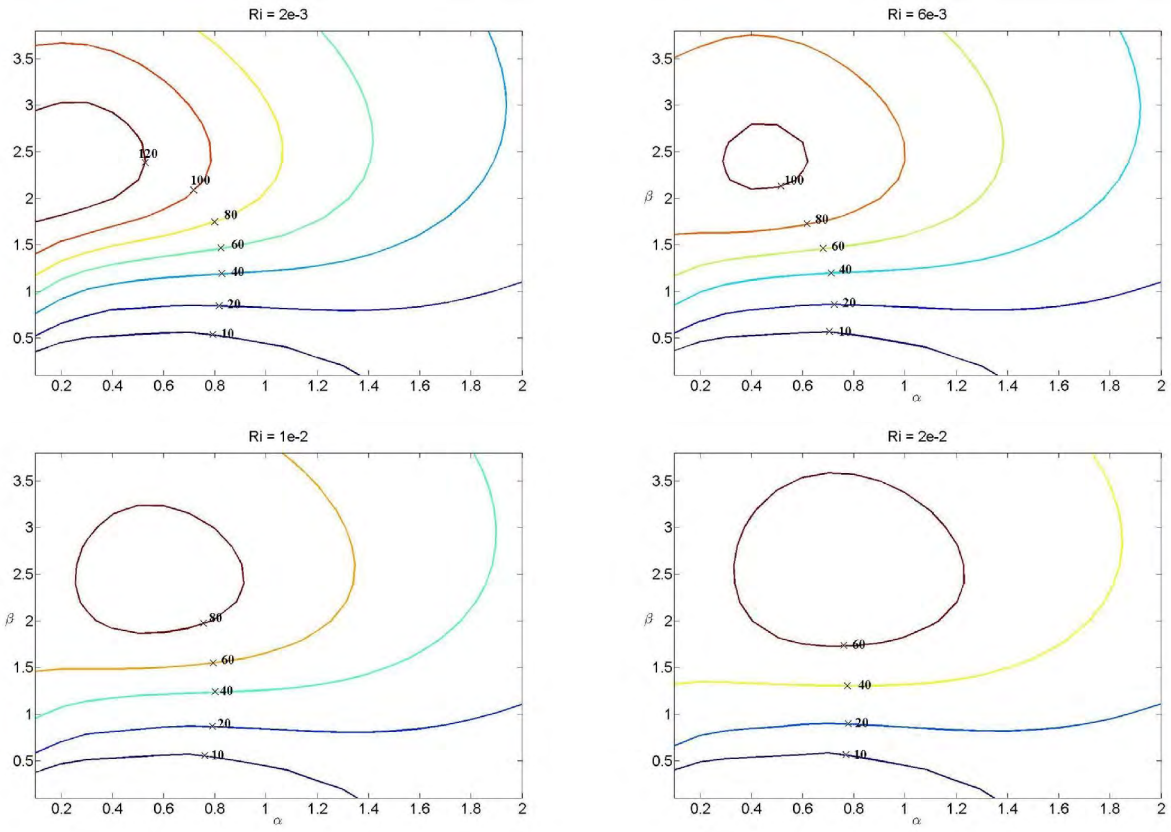

Figure 2-15: Contours of maximum energy amplification in the (α,β) plane for a laminar and stratified channel flow at Re=1000. Four cases at a different Richardson number are presented: top left figure, Ri=$2 \cdot 10^{-3}$; top right figure, Ri=$6 \cdot 10^{-3}$; bottom left figure Ri=$1 \cdot 10^{-2}$; and bottom right figure, $2 \cdot 10^{-2}$

Chapter 3.- Results and Discussion

In this chapter the complete problem of turbulence and stratification in a channel flow is tackled. Significant results are compared to the DNS information provided by García-Villalba & Del Álamo. These numerical simulations have been performed at a friction Reynolds number Re_τ=550 and at four different friction Richardson numbers, Ri_τ, (0, 60, 120 and 480). This chapter begins with a brief description of the governing equations, and continue with the analytical approximation for the turbulent eddy viscosity and thermal diffusivity that is taken to reproduce these profiles at the different Richardson numbers considered. The rest of the sections are dedicated to the analysis of the flow.

3.1 Governing equations

The general problem to be solved in this study is a turbulent and stratified flow in channel with the geometry described in the Introduction.

After linearizing Navier-Stokes and Energy equations, having taking into account the Boussinesq approximation and a y-dependant eddy viscosity, and applying the same mathematical procedures detailed in the preceding sections, the governing equations are reached and read:

$$\begin{aligned}
&\left[\left(\partial_t + U\partial_x\right)\Delta - U''\partial_x - \upsilon_t\Delta^2 - \left(2\upsilon_t'\partial_y\right)\Delta - \upsilon_t''\partial_{yy}\right]v = -\mathrm{Ri}\left(\partial_{xx}+\partial_{zz}\right)\rho \\
&\left[\left(\partial_t + U\partial_x\right) - \upsilon_t\Delta - \upsilon_t'\partial_y\right]\eta = -U'\partial_z v \\
&\left[\left(\partial_t + U\partial_x\right) - k_t\Delta - k_t'\partial_y\right]\rho = -\overline{\rho}'\, v
\end{aligned} \qquad (3.1)$$

It is noted that a thermal diffusivity variable with the vertical coordinate y is considered. The influence of this non-constant diffusivity is observed in the equation for the fluctuations of density where a new term in the derivative of the diffusivity appears (in comparison with the equation in section 2.3)

Numerical resolution of Ny=200 grid points has been used, which is enough to resolve the eigenfunctions for the smallest waves considered at a Reynolds number of 550. In order to determine this numerical resolution several test have been carried out with different number of grid points. These test proved that using a more detailed numerical resolution (than Ny=200) does not contribute to improve the results. Noticeable differences in the least damped eigenvalues and in the maximum energy amplification, G, were not found in computations with numbers of grid points higher

than 200. Moreover, a more detailed numerical resolution would have entailed a more expensive time demand in the computations[6].

3.2 Turbulent eddy viscosity and thermal diffusivity approximation.

When considering turbulence, the constant molecular viscosity used should be substituted by a variable turbulent eddy viscosity $\nu_t(y)$ to model the interaction of the perturbations with the background turbulence and to be able to separate small and large scales. The need of a variable thermal diffusivity is analogous.

In section 2 the Cess analytic approximation for the turbulent eddy viscosity is used. From this variable viscosity, the mean velocity profile is computed by integrating the mean Navier-Stokes equation in the streamwise direction. Since the presence of buoyancy changes the mean velocity profile of the flow, Cess formula can no longer be used.

The solution adopted is a modified Cess formula where not only the coefficients K and A must be fixed from numerical channel results but seven coefficients that changes the form of the polynomials in the approximation. The formula now reads:

$$\upsilon_t = \frac{1}{\mathrm{Re}}\left[\frac{1}{2}\left(1+a\left(by+cy^2\right)^2\left(d+ey+fy^2\right)^2\left(1-\exp\left(-gy\right)\right)^2\right)^{\frac{1}{2}}+\frac{1}{2}\right] \qquad (3.2)$$

where a, b, c, d e, f and g are the coefficients to be fixed.

The cases evaluated correspond to Re_τ=550 and Ri_τ=0, 60, 120 and 480, where DNS data is available from García-Villalba & Del Álamo (2008). The parameters are fixed by least-square fitting the mean velocity profile from the numerical channel results.

	Ri=0	Ri=60	Ri=120
a	600	600	590
b	5,274	6,139	5,269
c	-2,65	-3,089	-2,644
d	4,029	3,651	3,335
e	-5,922	-7,114	-6,592
f	2,976	3,571	3,301
g	22,07	-22,01	-22,02

	Ri=0	Ri=60	Ri=120
SSE	0,0006346	0,0008674	0,0009586
R-square	0,997	0,9933	0,9874
Adjusted R-square	0,9969	0,9931	0,9871
RMSE	0,00165	0,001863	0,001958

Table 3-1.- Value of the parameters of the modified Cess formula for the turbulent eddy viscosity. In the three cases Re=550. The table on the right shows the goodness of fit[7].

[6] Matrixes used in eigenvalue problem computations have a size of (3 Ny)x(3 Ny)

[7] The definition of the different parameters used to express the goodness of fit is the following:

a) Sum of Square Errors: $SSE = \sum_{i=1}^{N}\left(data - regression\right)^2$

The case of Re=550 and Ri=480 is not fit with enough accuracy with the modified Cess formula from above due to the flattening-shape of the turbulent eddy viscosity in the centre of the channel. Therefore a new polynomial that goes to zero in y=0 has been added to the formula, achieving a proper fit to the numerical results. Thus, the analytical approximation reads:

$$\upsilon_t = \frac{1}{\mathrm{Re}}\left[\frac{1}{2}\left(1+a\left(by+cy^2\right)^2\left(d+ey+fy^2\right)^2\left(1-y\right)^2\left(1-\exp\left(-gy\right)\right)^2\right)^{\frac{1}{2}}+\frac{1}{2}\right] \qquad (3.3)$$

	Ri=480
a	600
b	4,666
c	-2,342
d	3,283
e	-6,11
f	3,057
g	-22,02

	Ri=480
SSE	0,000341
R-square	0,9901
Adjusted R-square	0,9898
RMSE	0,001168

Table 3-2.- Value of the parameters of the turbulent eddy viscosity formula for Re=550 and Ri=480. The table on the right show the goodness of fit.

An analogous analytical approximation is used for the thermal diffusivity. Following the same procedures as for the turbulent eddy viscosity, the value of the parameters have been fixed. Table 3.3 and Table 3.4 shows them.

$$k_t = \frac{1}{\mathrm{Pr}\,\mathrm{Re}}\left[\frac{1}{2}\left(1+a\left(by+cy^2\right)^2\left(d+ey+fy^2\right)^2\left(1-\exp\left(-gy\right)\right)^2\right)^{\frac{1}{2}}+\frac{1}{2}\right] \qquad (3.4)$$

	Ri=0	Ri=60	Ri=120
a	600	600	372,5
b	4,475	4,84	5,176
c	2,254	-2,436	-2,601
d	3,879	3,219	3,382
e	-5,635	-6,28	-6,706
f	2,841	3,152	3,361
g	-21,98	-22	-22
dρ/dy(-1)	-8,223	-3,4740	-2,7017

	Ri=0	Ri=60	Ri=120
SSE	0,0005883	0,0009648	0,0002749
R-square	0,9962	0,9925	0,9972
Adjusted R-square	0,9961	0,9924	0,9972
RMSE	0,001534	0,001964	0,001049

Table 3-3.- Value of the parameters of the modified Cess formula for the thermal diffusivity. In the three cases Re=550. The table on the right shows the goodness of fit.

---

b) R-square=SSE/s^2 , where s means the variance in the data. When R-square approaches unity, regression approaches a perfect fit.

c) Adjusted R-square= $\frac{SSE/(n-p-1)}{\sigma^2/(n-1)}$, where n is the sample size and p is the total number of regressors. Adjusted R-square is a modification of R-square that adjusts for the number of explanatory terms in a model. Unlike R-square, the adjusted R-square increases only if the new terms improves the model more that would be expected by chance. Adjusted R-square will always be less than or equal to R-square.

d) Root Mean Square Error: RMSE, is a measure of total error defined as the square root of the sum of the variance and the square of the bias.

$$k_t = \frac{1}{\mathrm{Pr}\,\mathrm{Re}}\left[\frac{1}{2}\left(1+a\left(by+cy^2\right)^2\left(d+ey+fy^2\right)^2\left(1-y\right)^2\left(1-\exp\left(-gy\right)\right)^2\right)^{\frac{1}{2}}+\frac{1}{2}\right] \qquad (3.5)$$

	Ri=480
a	610
b	3,755
c	-1,886
d	2,986
e	-5,539
f	2,776
g	-21,99
dρ/dy(-1)	-1,6743

	Ri=480
SSE	0,0001557
R-square	0,9959
Adjusted R-square	0,9958
RMSE	0,0007893

Table 3-4.- Value of the parameters of the thermal diffusivity formula for Re=550 and Ri=480. The table on the right show the goodness of fit.

The benefit of using the analytical approximation both in the viscosity and diffusivity lies in the smoothness of the functions. Thus, when computing the derivatives of the velocity, viscosity and diffusivity, which are introduced in the equations, the functions are smooth enough for a proper numerical behaviour. At first, it was tested to use directly the DNS data distributions but the peaky-shape got in the derivatives led to numerical instability. The reason is the appearance of spurious eigenvalues, which are unstable, whereas with smooth functions for the viscosity and diffusivity those non-physical eigenvalues do not appear. Therefore, the solution adopted is to use a analytical approximations based on the Cess formula. And although the fit with the DNS data distributions is not perfect, it reproduces the main characteristics of the profiles.

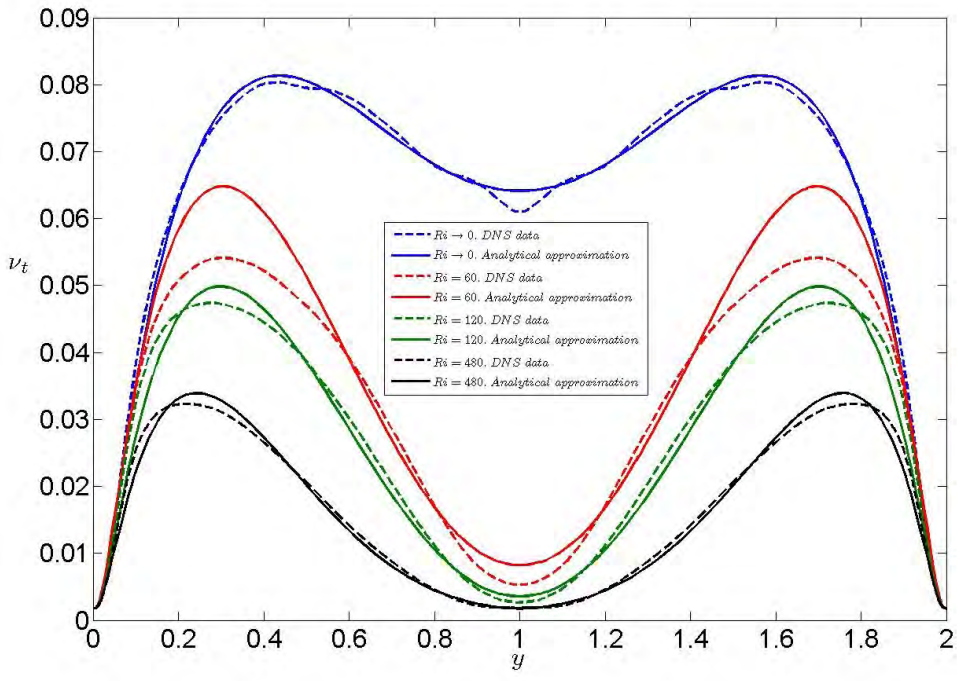

Figure 3-1.- Comparison between the turbulent eddy viscosity used in this study (analytical approximation) and the DNS data. The four cases are at Re=550.

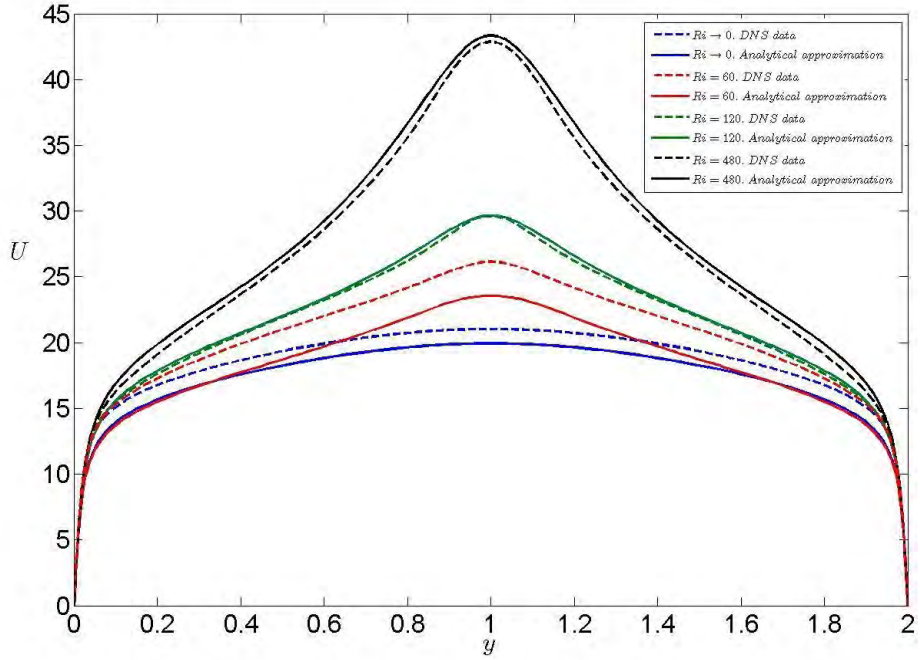

Figure 3-2.- Comparison between the mean velocity profile used in this study (analytical approximation) and the DNS data. The cases represented are the same as in Figure 3-1

3.3 Comparison between non-stratified and Ri →0 at Re=550

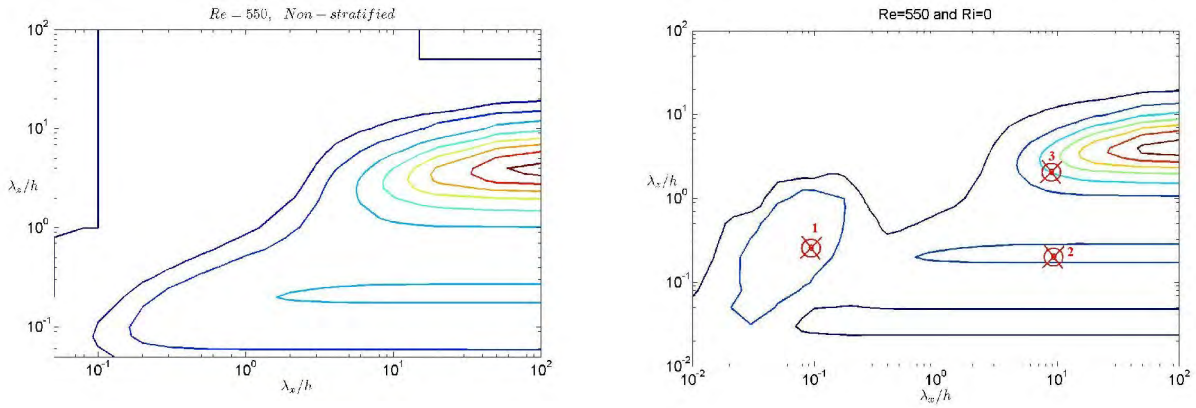

Figure 3-3: Contours of maximum energy amplification, G, in the λ_x-λ_z plane. Figure on the left is the non-stratified case at Re=550, with levels [1 1.5 2(+1)8] from blue to red. Figure on the right corresponds to the stratified case at Ri→0 and Re=550, with levels 1(+1)8 from blue to red. Points highlighted are: 1 (λ_x=0.08h, λ_z=0.3h), 2(λ_x=10h, λ_z=0.2h), 3(λ_x=,10h λ_z=2h).

A first approach to a stratified and turbulent flow can be given by analyzing Figure 3-3. There it is represented two energy maps which correspond to the non-stratified case and the Ri→0 case both at Re=550. Differences between them must be expected to come from buoyancy forces.

As Ri→0, Orr-Sommerfeld and energy equation are weakly coupled, but it does exist a relationship between them due to the energy's forces term $-\rho_0' v$ in the right

hand of the equation. This term causes the interaction among the three components of the kinetic energy and the potential energy.

The most relevant difference between the two maps is the appearance of energy growth for $\lambda_z>\lambda_x$ in the small scales. A detailed study of each component of the energy done in point 1 (defined in Figure 3-3) reveals that the disturbance is entirely due to the potential energy, that is to say, in density perturbations. This agrees with the fact of not having appeared in the non-stratified case.

Two other points have been studied in detail. Points 2 and 3 correspond to the two local maxima in energy found in the turbulent and non-stratified case for large λ_x. These maxima are linked to the small-scale and large-scale structures, respectively, observed in numerical results and experiments.

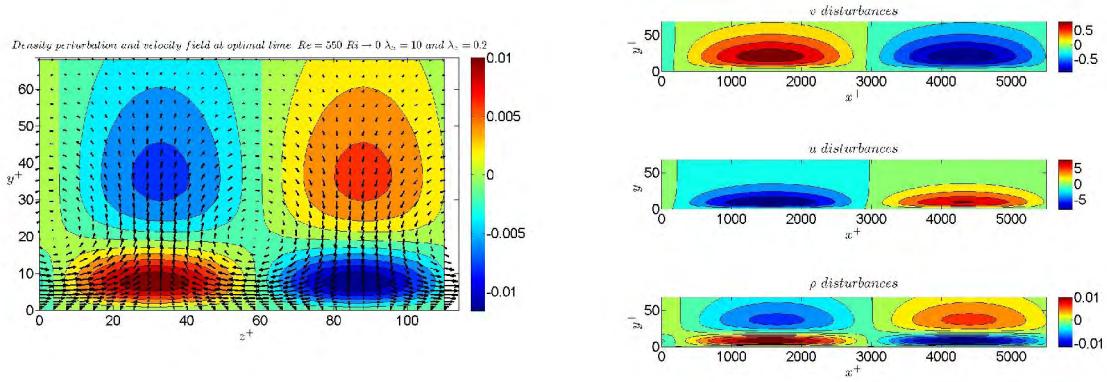

Figure 3-4: Velocity field and density perturbation in the time of most amplified energy at Re=550, Ri→0, λ_x=10, λ_z =0.2. Figure on the left corresponds to the y-z plane in wall units, and figure on the right to the x-y plane in wall units as well.

It is remarkable in Figure 3-4 that near the wall the component of the velocity in the streamwise direction is one order of magnitude higher that the transverse velocity. This suggests the presence of the near-wall streaks, structure that characterized the first local maxima in the turbulent and non-stratified flow (Smith & Metzler 1983), and that is reproduced as well in the weakly stratified case.

The velocity field of point 3 (λ_x=10 and λ_z =2) is composed by two counter-rotating vortices which occupy the whole channel. Again this structure is similar to the one obtained in the non-stratified flow and corresponds to the large global structures documented by del Álamo & Jiménez (2003) and del Álamo *et al*. (2004)

Comparing the two energy maps it is noted the near coincidence of both, except the potential modes. Energy levels are similar and are reached with the same width structures.

The dynamics of the present optimal solutions at Ri→0 are analysed in Figure 3-5, which shows the streamwise and transverse components of the energy growth, $G_u=u^2(t)/[2q(0)]$ and $G_{v,w}=[v^2(t)+w^2(t)]/[2q(0)]$. The data are presented for λ_x =20h and Re_τ=550, and are given as functions of λ_z and of time. The latter is normalized with the instant of maximum energy amplification, t_m. Potential energy in this size of λ_x does not play a relevant role. Therefore, a similar behaviour to the unstratified turbulent flow (see figure 2.9) is expected. In Figure 3-5, it is seen that, initially, almost all the kinetic energy is contained in the transverse motions that decay generating streamwise velocity fluctuations. At $t\approx t_m$, G_u reaches its maximum. Its value is approximately equal to the highest value of G in Figure 3-3, indicating that the energy growth in the present model for Ri→0 occurs mainly in the streamwise component. These results agree with Del Álamo & Jiménez (2006)

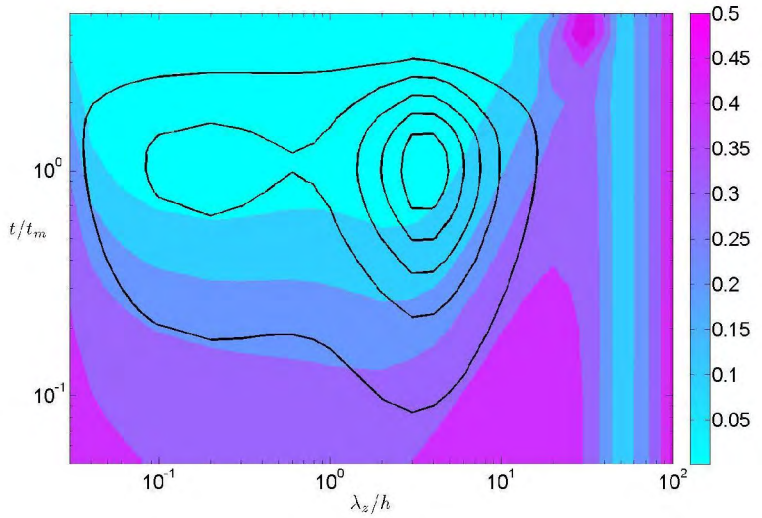

Figure 3-5: Component-wise energy amplification as a function of λ_z/h and t/t_m; $\lambda_x=20h$; Re=550; Ri→0; the line contours come from the streamwise component, G_u, and the levels represented are 1(+1)5; the coloured contours come from the transverse component, $G_{v,w}$ and the levels represented are 0.1(+0.1)0.5.

3.4 Energy maps at increasing Ri number.

In this section, energy maps at three Ri number (Ri=60, 120 and 480) are compared and studied, identifying the common structures that appear and its evolution as Ri number increases. Time in all the cases is the optimal time at which the maximum amplification of energy is given. Results are contrasted with DNS data available from García-Villalba & Del Álamo (2008) at the same Ri number. Reynolds number is for all cases of 550. The numerical resolution is of Ny=200 grid points, which are enough to resolve the eigenfunctions for the smallest waves considered at that Reynolds number.

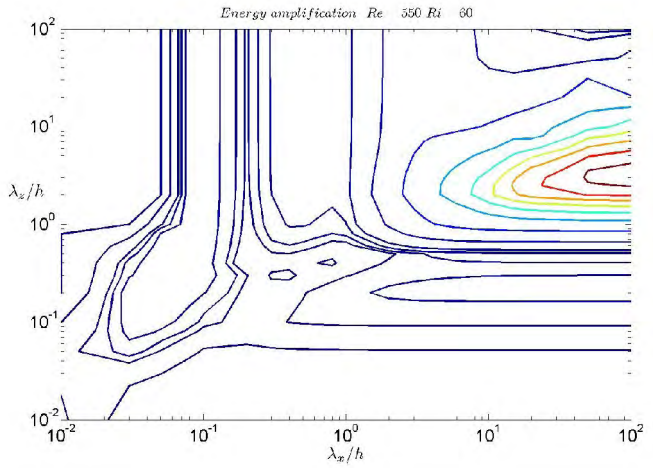

Figure 3-6: Contours of maximum energy amplification, G, in the λ_x-λ_z plane. Ri=60 and Re=550, with levels [1 1.5 2 2.2 2.5 3 5 10(+10)70] from blue to red.

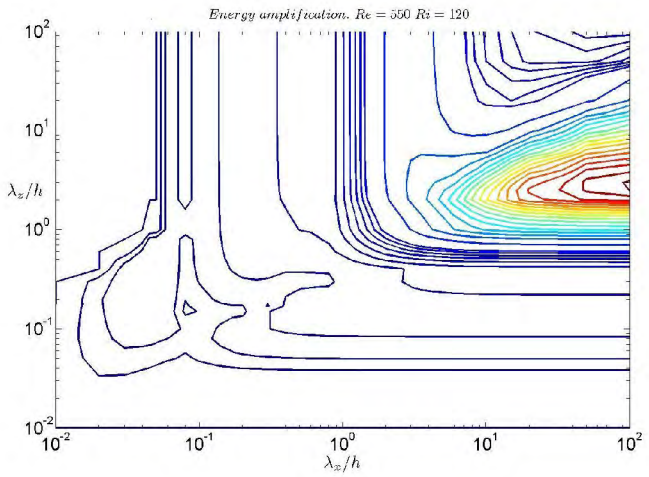

Figure 3-7: Contours of maximum energy amplification, G, in the λ_x-λ_z plane. Ri=120 and Re=550, with levels [1 1.5 2(+1)10 15(+5)85] from blue to red.

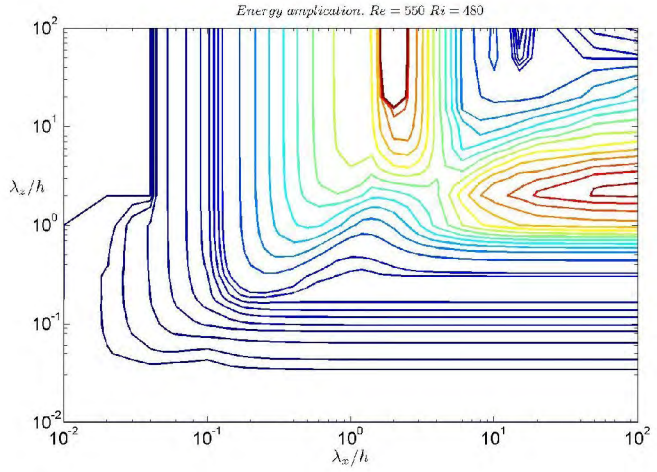

Figure 3-8: Contours of maximum energy amplification, G, in the λ_x-λ_z plane. Ri=120 and Re=550, with levels [1 1.5 2(+1)10 15(+5)80] from blue to red.

Concentrating on the general shape of these maps, our attention is attracted first by the energy growth that occurs for $\lambda_z>\lambda_x$. This fact does not happen to non-stratified flows. Thus, it can be considered as an element to characterize stratified flows in a channel. The first hint of this behaviour is given at Ri =0, where at small scales takes place a bubble of energy growth for spanwise wavelengths higher than streamwise ones. This bubble expands at Ri=60 towards long-scale λ_z as Figure 3-6 shows.

Focusing on point 1, which is defined in Figure 3-3, it is seen the evolution of the velocity perturbation field and the density fluctuations of a structure with such wavelengths that at Ri=0 is inside that growth bubble described below. However, the structures in this point studied will not be the dominant ones since their energy amplification is smaller than in other zones. At Ri=60 it is found the same pair of counter-rotating vortices that appears in the bottom wall as it happens at Ri=0. A different behaviour occurs at high Richardson number where the strong perturbation is localized in the centre of the channel, as Figure 3-9 shows:

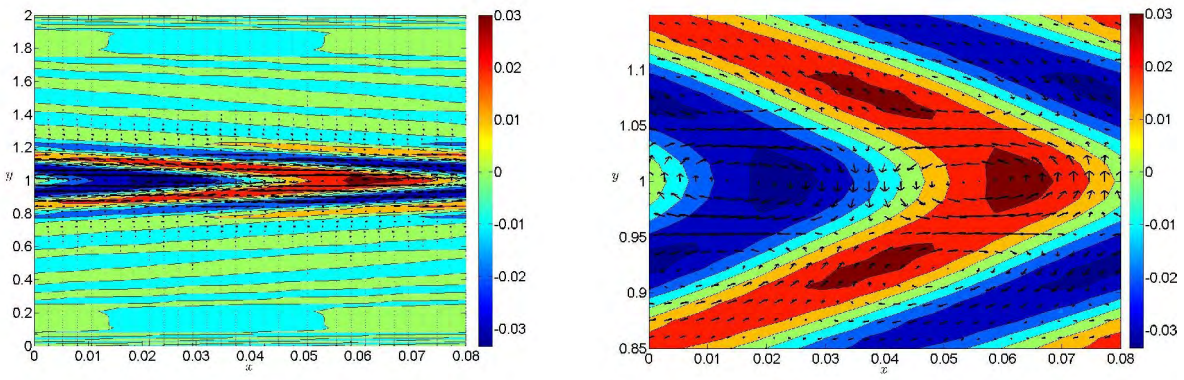

Figure 3-9: Perturbation velocity field and density fluctuation in the x-y plane at Ri=480, Re=550, λ_x =0.08h and λ_z =0.3h. Figure on the left comprises the whole height of the channel and the size of the wavelength in the x-direction, and figure on the right is a zoom-sight of the centre of the channel.

The velocity field of this case is a more complex one, and it is made up of three pair of counter-rotating vortices in a small band in the centre of the channel.

Point 2, defined in Figure 3-3, reflects at Ri=60 and 120 the same structure that was commented in the preceding section and that corresponds to the near-wall streaks. In both cases the magnitude of the component of the perturbation velocity in the streamwise direction is an order higher than v and w, respectively, at the time of maximum energy amplification. At Ri=480 this structure is not caught in this point. This difference will be discussed and explained when analysing the different contributions of the energy.

The appearance of Point 3, defined in Figure 3-3, changes completely as the Richardson number increases. It is important the study of this case since its structures are prevalent in the flow due to the high energy amplification reached. At least until Ri=120 large structures in the x-direction and with a width of around 3 are dominant. At Ri=0 it was observed two counter-rotating vortices acting in the whole height of the channel. In the other three cases (Ri=60, 120 and 480) what the perturbation velocity field shows are two pair of counter-rotating vortices, one acting in the upper half of the channel and the other one in the bottom half. It is observed a slightly separation of the flow in the centre of the channel into two anti-symmetric perturbations. This fact is confirmed in the DNS distributions. It is noticed as well how this perturbation is distorted with a higher Ri number.

In the DNS (Figure 3-11) it is observed, for the case Ri=0, how vortical structures occupy the whole channel. They are concentrated on both walls and distributed along the channel, even crossing the centre of it. On the other hand, this behaviour changes as the Richardson number increases. It is noticeable at Ri=480 the separation that happens in the centre of the channel. Vortical structures are more marked in this case, being quite dominant in the upper and bottom half on the channel (and not only very intense near the walls, as in Ri=0), but at the centre these structures disappear, setting up a barrier between both halves. As it was noted above, this behaviour agrees with the results of the linear model and suggests that the genesis of those structures is captured at least approximately by our model.

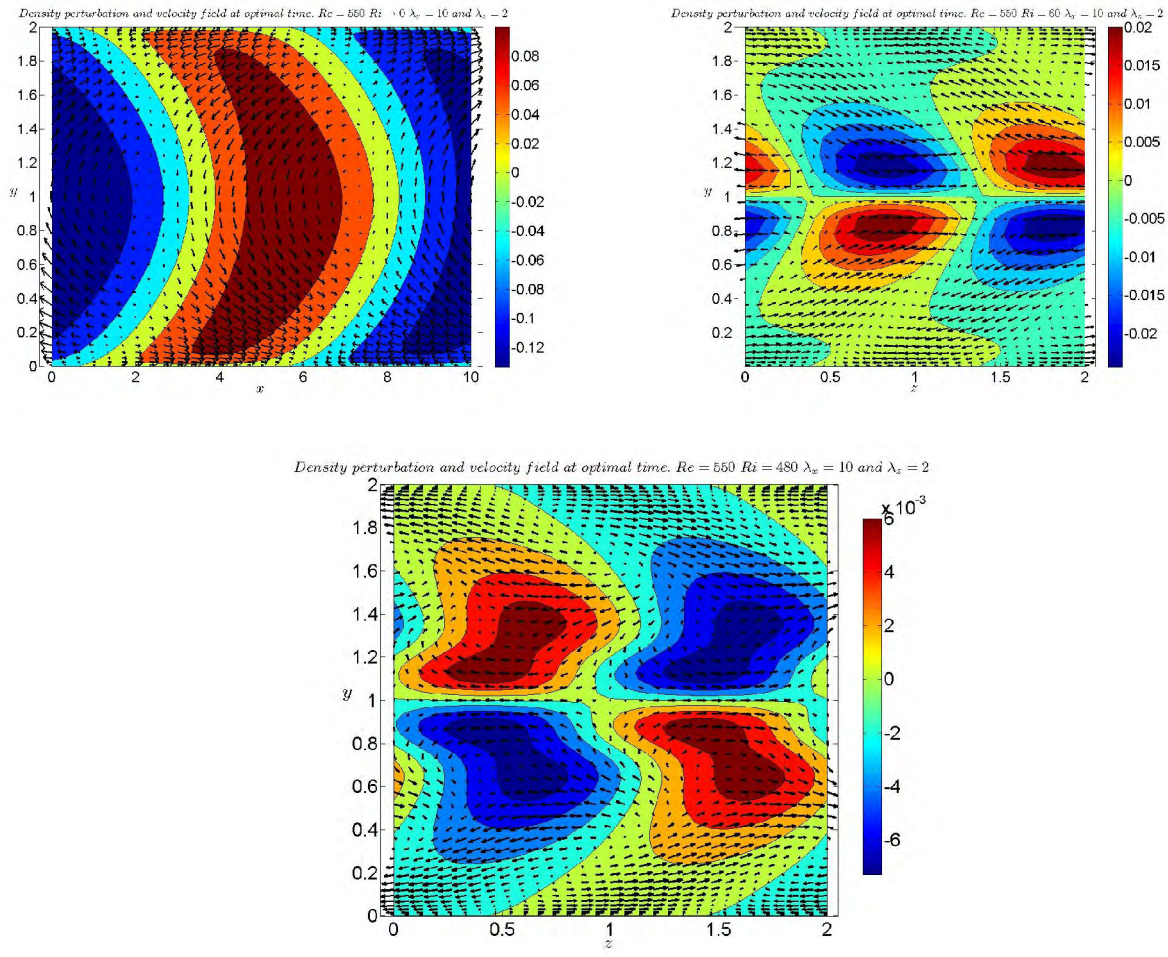

Figure 3-10: Perturbation velocity field and density fluctuation in the z-y plane at Re=550, λ_x =10h and λ_z =2h. Figure on the top left corresponds to Ri→0 and figure on the top right to Ri=60. Figure on the bottom is the case Ri=480.

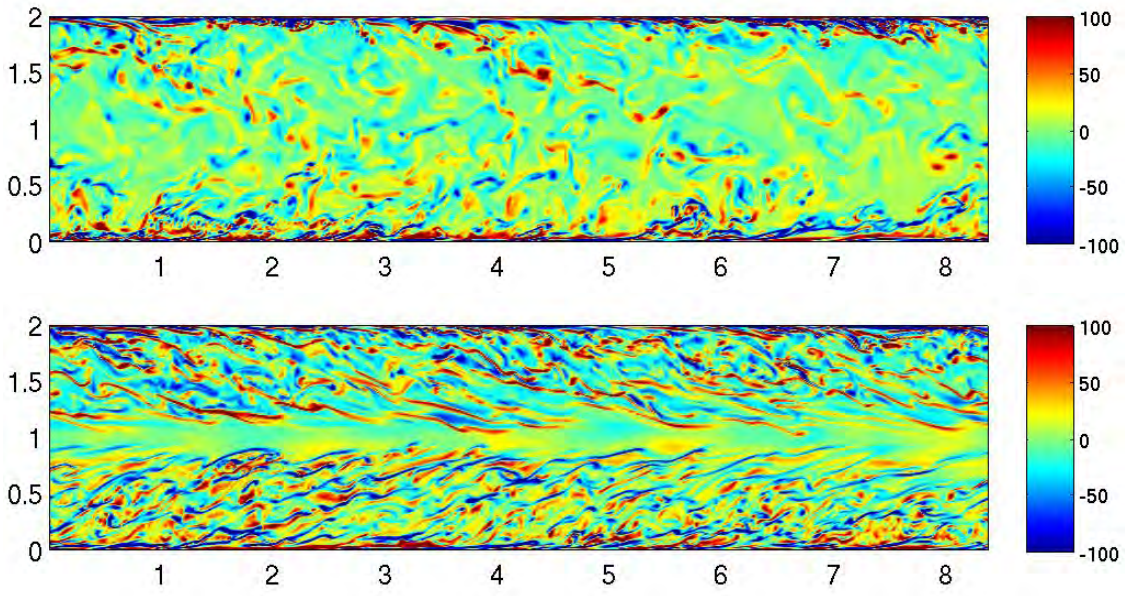

Figure 3-11: Spanwise vorticity in the (x-y) plane at Re=550 from DNS. Figure on the top is at Ri=0 and figure on the bottom at Ri=480. Pictures taken from García-Villalba & Del Álamo (2008)

A similar study than in the preceding section has been made about the components of the energy in the case Ri=480 and with the same λ_x=20h. Figure 3-12 shows that the maximum energy amplification is still related to the streamwise component of the velocity, that reaches its maximum at the optimal time t≈t_m. The component u of the velocity is, as in the case Ri→0, triggered by the transverse motion through the Squire's forcing term (not shown). It is also noted the appearance of potential energy as the dominant one in small-scale of the width (around 0.2 h).

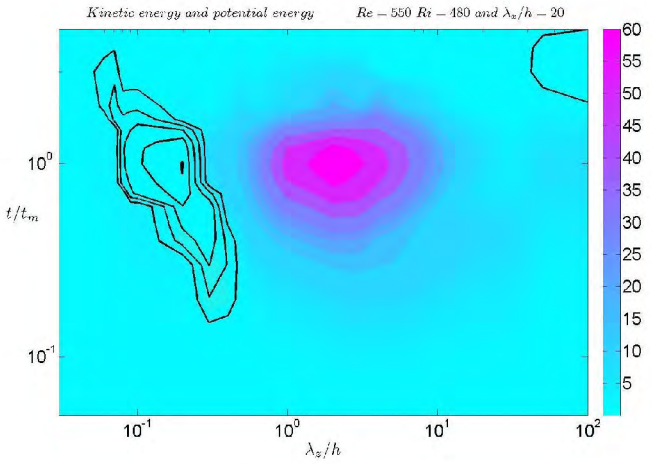

Figure 3-12: Component energy amplification as a function of λ_z/h and t/t_m; λ_x=20h; Re=550; Ri=480; the line contours come from the potential energy and the levels represented are 1(+1)5; the coloured contours come from the kinetic energy and the levels represented are 5(+5)60.

3.5 Internal waves

At the end of the preceding section, it was highlighted the fact that for small-scale in the width (around 0.2 h), the main component that contribute towards energy amplification is the potential energy. With this result in mind, present case has been computed to see how the perturbation velocity field and density fluctuations look like in conditions where the buoyancy forces are dominant. Buoyancy forces arise as a result of variations of density in a fluid subject to gravity. One of its consequences is the appearance of internal waves in the bosom of the fluid. It is interesting to show Figure 3-13 where this behaviour of the fluid can be clearly seen.

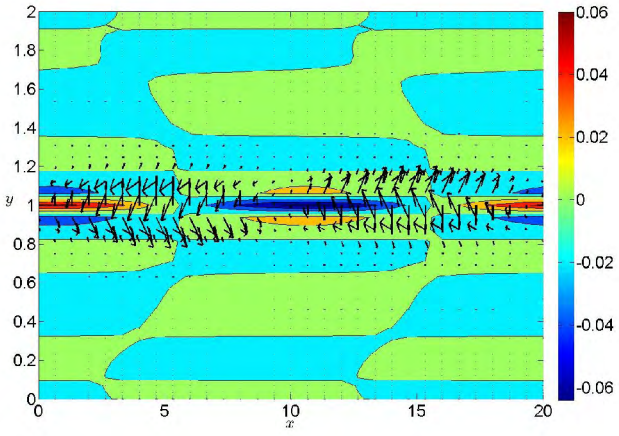

Figure 3-13: Perturbation velocity field and density fluctuation in the x-y plane at Re=550, Ri=480, λ_x =20h and λ_z =0.2h

In a continuously stratified and no-viscous flow the linearized energy equation takes the simple form $\partial_t \rho = -\overline{\rho}' v$, which indicates that density variations at a fixed point are due entirely to the vertical displacement, and are 90° out of phase with the vertical velocity. When adding the viscous terms this relation of phase slightly changes and it remains around 90° (Turner, 1973). Thus, an easy way of verifying the presence of internal waves in the fluid is by checking that the density fluctuation are nearly 90° out of phase with the vertical velocity. This can be observed in the numerical simulations by García-Villalba & Del Álamo (2008) as Figure 3-14 shows

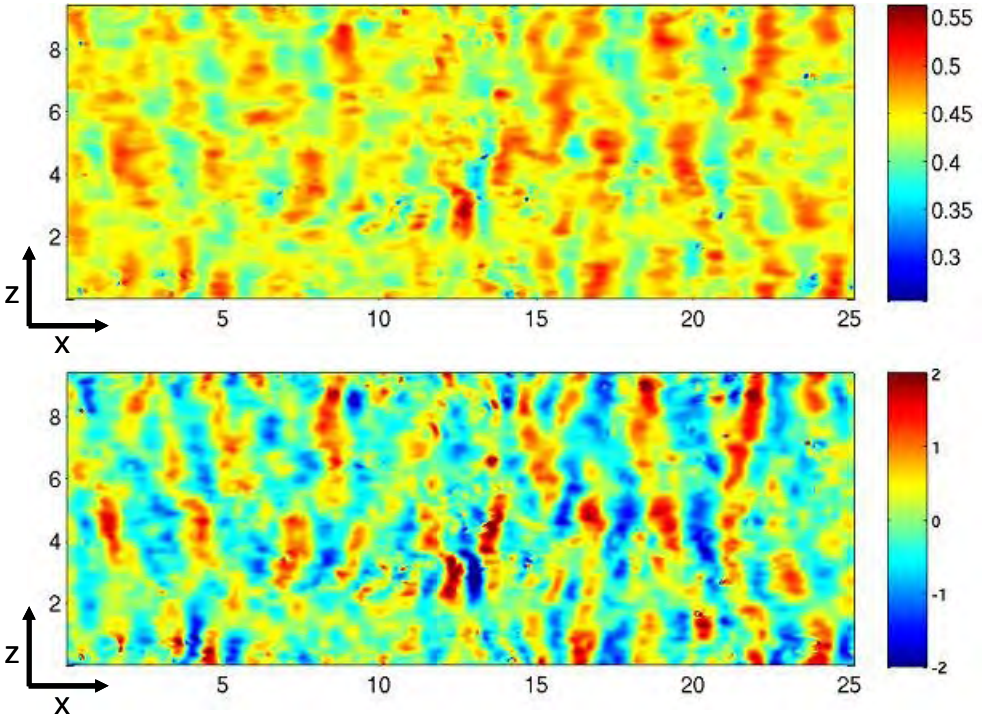

Figure 3-14: Internal waves in the centre of the channel (x-z plane) at Ri=480 and Re=550. Figure on the top represents the density and figure on the bottom the vertical velocity. Figures taken from the DNS by García-Villalba & Del Álamo (2008).

The same phenomenon shows the case presented at the beginning of this section. In order to see it properly, vertical velocity and density in the centre of the channel have been plotted. It is observed this nearly 90° out-of-phase between the two variables and, consequently, another evidence that it is indeed an internal wave.

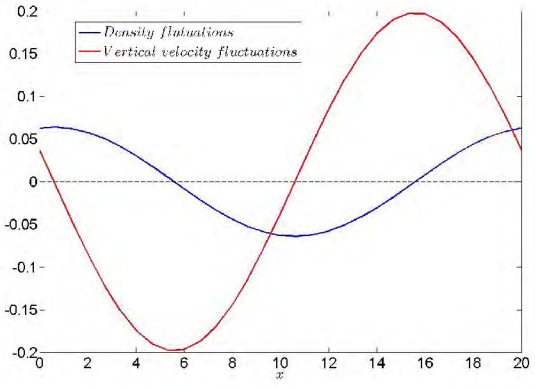

Figure 3-15: Perturbation vertical velocity (red line) and density fluctuations (blue line) in the centre of the channel along the streamwise direction at Re=550, Ri=480, λ_x=20h and λ_z=0.2h.

3.6 Component energy analysis.

In this section the objective is to study in depth the three cases which where defined in Figure 3-3 and whose sizes are detailed in Table 4-5. The aim is to see the distribution in each component of the energy amplification at the time of its maximum and at the initial time. In this way the components of the kinetic energy or potential energy at the initial time that yield to the maximum amplification will be observed, as well as how this energy at $t=t_m$ is shared out. Each case has been explored for the four Richardson number Ri=0, 60, 120 and 480, and for Re=550.

	λ_x/h	λ_z/h
Case 1	0.08	0.3
Case 2	10	0.2
Case 3	10	2

Table 3-5: Table where the three cases of component energy study are defined.

Case 1 is essentially caused by the potential energy as Figure 3-16 shows. The potential energy in this small-scale is the one who triggered itself and amplify its magnitude. This is a marked behaviour for Ri→0 and Ri=60. As the Richardson number increases, there is a small percentage of transverse motion energy at the initial time that yields to the maximum amplification; anyway, the main one keeps being due to density fluctuations. In any case, at optimal time all the energy is practically potential. However, as it is shown in Figures 3-(6-8), these sizes do not contain a great amount of energy. Therefore the corresponding structures are not the prevalent in the flow.

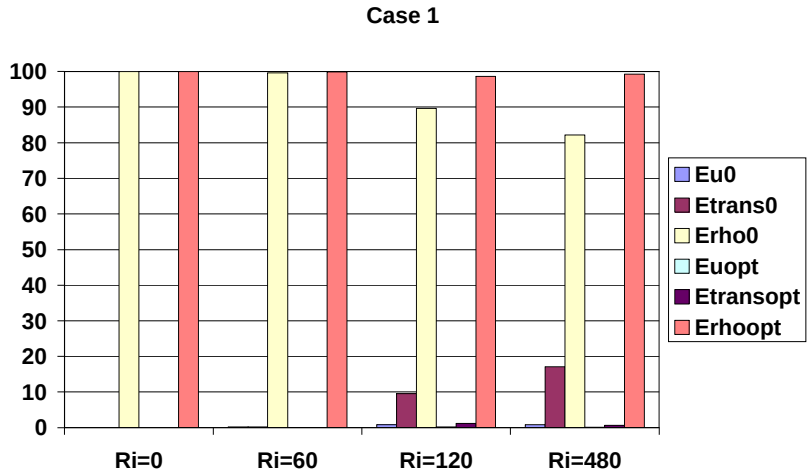

Figure 3-16: Case 1. Bar graph of the three components of the kinetic energy and potential at both times, initial time and time for the maximum energy amplification. The legend of colours corresponds to: violet (streamwise motion energy at initial time), maroon (transverse motion energy at initial time), yellow (potential energy at initial time), blue (streamwise motion energy at optimal time), red (transverse motion of energy at optimal time) and orange (potential energy at optimal time).

Observing Figure 3-17, it can be noted that in case 2 for Ri≤120 the distribution of energy of the eigenfunctions that yields to the maximum amplification comes the majority from transverse motion energy and a small percentage (around 10%) of streamwise motion energy. It is almost fully transformed into kinetic energy in the x-direction. This structure corresponds to the near-wall streaks, which have been found in numerical simulations (Robinson 1991). This transfer of energy from the transverse

motion to the streamwise one can be explained through the forcing term in Squire's equation: $-U'\partial_z v$.

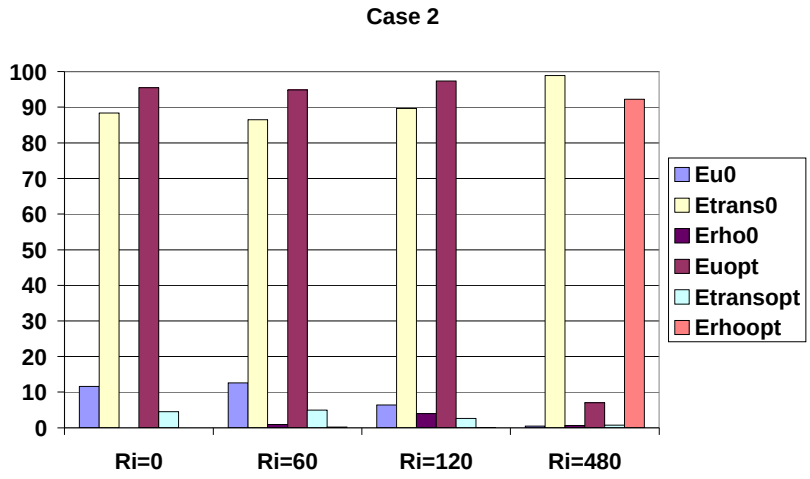

Figure 3-17: Case 2. Bar graph of the three components of the kinetic energy and potential at both times, initial time and time for the maximum energy amplification. The legend of colours is the same as in Figure 3-16.

At Ri=480 the behaviour of the fluid changes, and although at initial time most of the energy is contained in the transverse motion, it is then transferred to the potential energy. This result agrees with Figure 3-12 where the components of the energy amplification are plotted. Keeping the same size of the structure in the streamwise direction, tests were made to look for an analogous behaviour of the flow (as in Ri=0, 60 and 120) in a wide range of λ_z. A similar case is found for λ_z=0.07h, that is to say, the near-wall streaks decreases in width (from 0.2h to 0.07h) as the Richardson number increases. This agrees remarkably well with the results of the DNS carried out by García-Villalba & Del Álamo (2008), as Figure 3-18 shows.

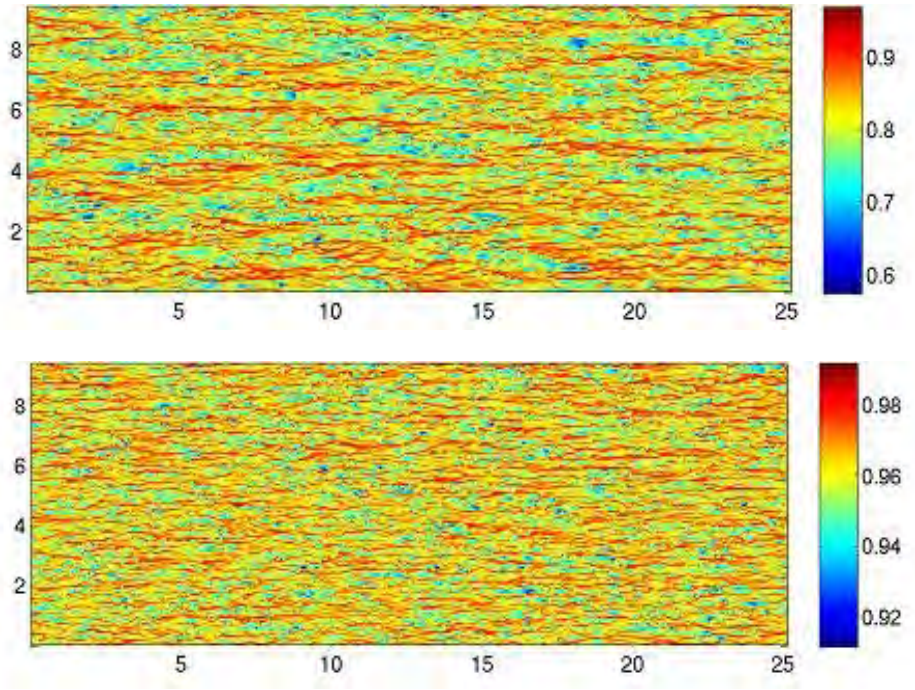

Figure 3-18: Density fluctuations very close to the wall in the plane x-z. Picture from above corresponds to Ri=0 and picture from below to Ri=480. Both pictures from the DNS by García-Villalba & Del Álamo (2008) at Re=550.

The amplification energy of the third case is much greater than the two preceding. Therefore, structures related to these scales are dominant in comparison with the others. Figure 3-19 shows how the transfer of energy at Ri→0 is basically from the transverse motion to the streamwise motion. However, this behaviour changes as the Richardson number increases in such a way that now the energy that triggers the maximum amplification is the potential energy, remaining the streamwise motion one as the prevalent (more than 90%) at the optimal time. Therefore, small perturbation in density produce a significant growth in the x-component of the velocity.

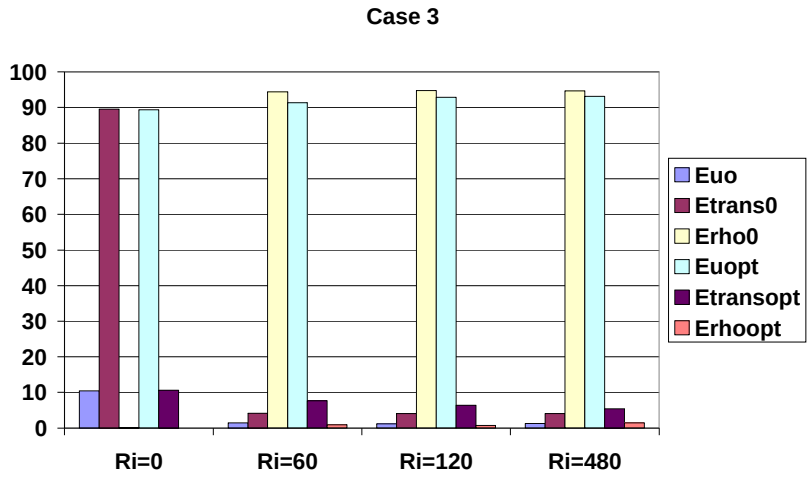

Figure 3-19: Case 3. Bar graph of the three components of the kinetic energy and potential at both times, initial time and time for the maximum energy amplification. The legend of colours is the same as in Figure 3-16.

3.7 Analysis in the limit $\beta = 0$.

An interesting object of analysis lies in the limit $\beta = 0$, where the widths of the structures are so big ($\lambda_z \to \infty$) that the flow behaves as if it was two-dimensional (only acting in the x-y plane). In a non-stratified flow, it has been seen that energy growth occurs for $\lambda_x > \lambda_z$; therefore this limit contains no information for that case. However, one of the characteristics of a stratified flow, which is moreover reinforced as Ri increases, is the appearance of growth for $\lambda_z > \lambda_x$. Thus, a study of the limit $\beta = 0$ can give us information about the influence of stratification in a channel flow.

A comparison between the non-stratified flow and weakly stratified one is shown in Figure 3-20. There it can be noticed how the growth of the non-stratified case is negligible in the limit $\beta = 0$. Thus, it is in keeping with the non-growth of energy that is expected in this case for $\lambda_x > \lambda_z$. When Ri→0 a peak of energy amplification appears in the small-scale ($\lambda_x \approx 0.1h$); analysing its energy distribution it is found that the kinetic energy does not take part, and it almost only concern to the potential energy, all the energy is contained in the density fluctuations. As stratification increases, energy growth begins to be considerable. For Ri=60, there are three local maxima in G. The first two maxima are directly linked to density fluctuations while perturbation velocity does not intervene. In Figure 3-21 a representation of the velocity field and the density perturbation can be seen. There, internal waves can be clearly identified. On the other hand, the third maximum, which is the highest peak, is triggered both for streamwise velocity and potential energy. At the optimal time most of the energy is kinetic but it also contain some not negligible potential energy (around 20%), which has grown in comparison to the initial one. In this peak, velocity field is composed by a pair of counter-rotating vortices in the centre of the channel.

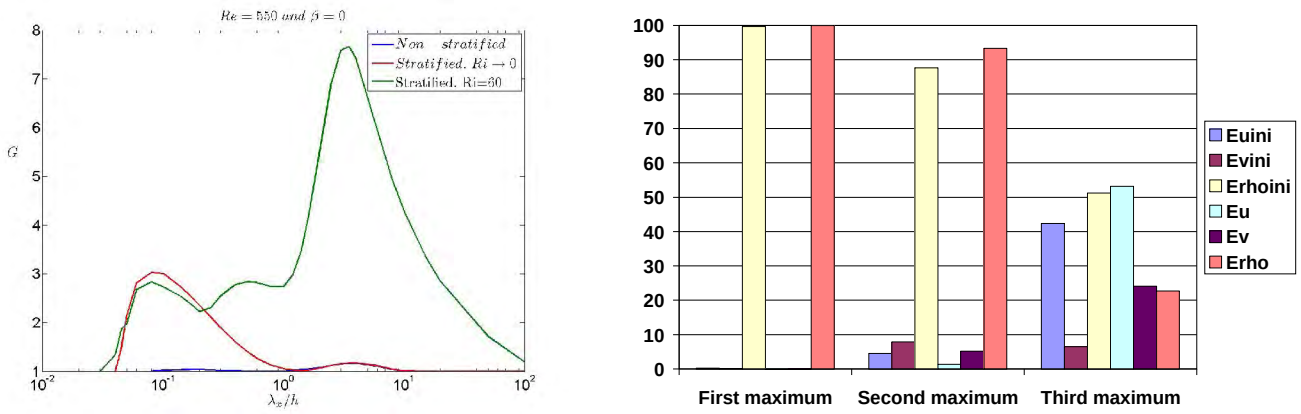

Figure 3-20: Maximum energy amplification in function of λ_x/h for Re=550 and β=0. Three cases have been plotted in the picture on the left: non-stratified flow (blue), stratified flow with Ri→0 (red) and stratified flow with Ri=60 (green). Picture on the right shows the energy distribution of the three energy peaks in the case Ri=60 at the initial and optimal time. The coloured legend is: violet (streamwise motion energy at t_0), maroon (vertical motion energy at t_0), yellow (potential energy at t_0), blue (streamwise motion energy at t_m), red (vertical motion energy at t_m), orange (potential energy at t_m)

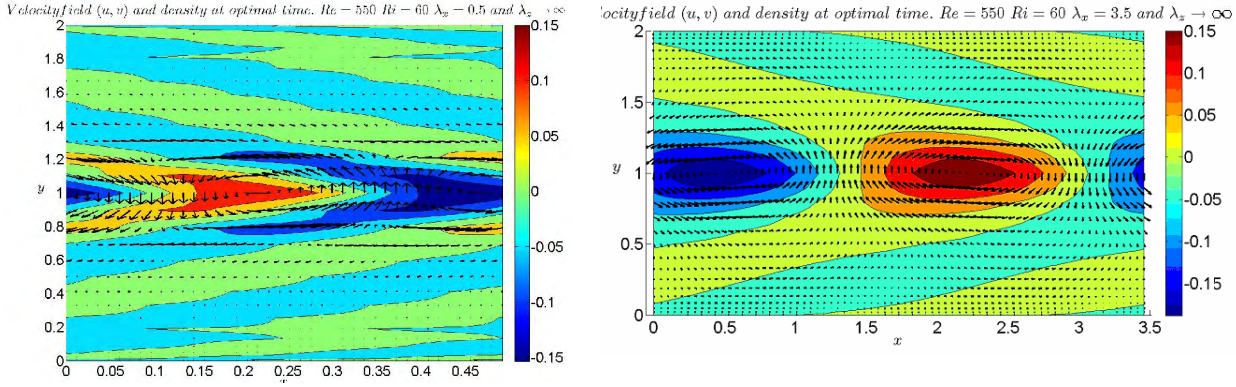

Figure 3-21: Perturbation velocity field and density fluctuations at Re=550, Ri=60 and β=0. Picture on the left corresponds to λ_x =0.5h (second G maximum) and picture on the right to λ_x =3.5h (third G maximum)

At Ri=120 phenomena increases. There are, in this case, four peaks in the energy amplification, G, each of one corresponding to a different mode of the flow. The first two local maxima and the last one are the evolutions of those three peaks found at Ri=60 (the distribution of energy are analogous in these sizes to the ones shown in Figure 3-20). It is significant that the size of G has risen to the double of the magnitude at Ri=60. A new peak in energy appears with a size in the streamwise direction of around 0.8h. It is noted that the distribution of energy is quite different to the rest of the energy peaks. In this case, at initial time most of the energy is kinetic in the streamwise motion, and it is fully transferred to potential energy at optimal time. When plotting the velocity field and density fluctuation at optimal time in this case, Figure 3-23, it is found a complex behaviour of the velocity. Four pairs of counter-rotating vortices are acting in the centre of the channel, and they are distributed into wakes of high and low density.

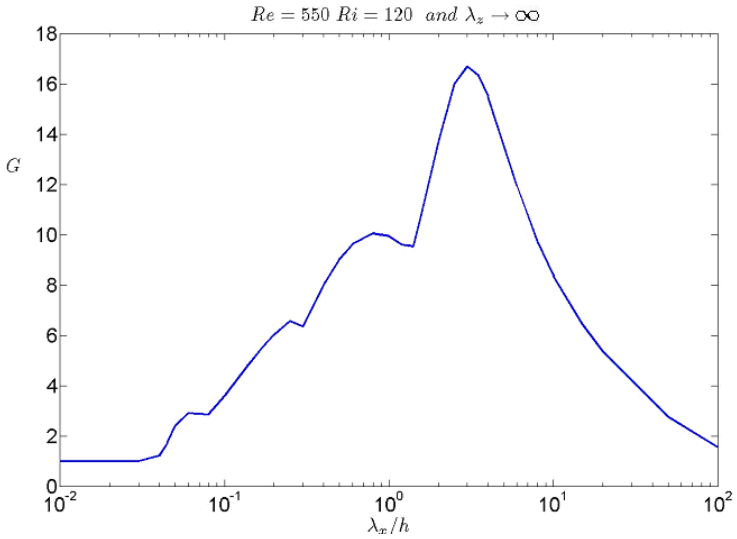

Figure 3-22: Maximum energy amplification in function of λ_x/h for Re=550, Ri=120 and $\beta=0$

%	t_0	t_{opt}
E_u	86	0.65
E_v	13.01	0.31
E_ρ	0.99	99.04

Table 3-6: Component energy distribution at initial and optimal time for Re=550, Ri=120, λ_x =0.8h and $\lambda_z \to \infty$

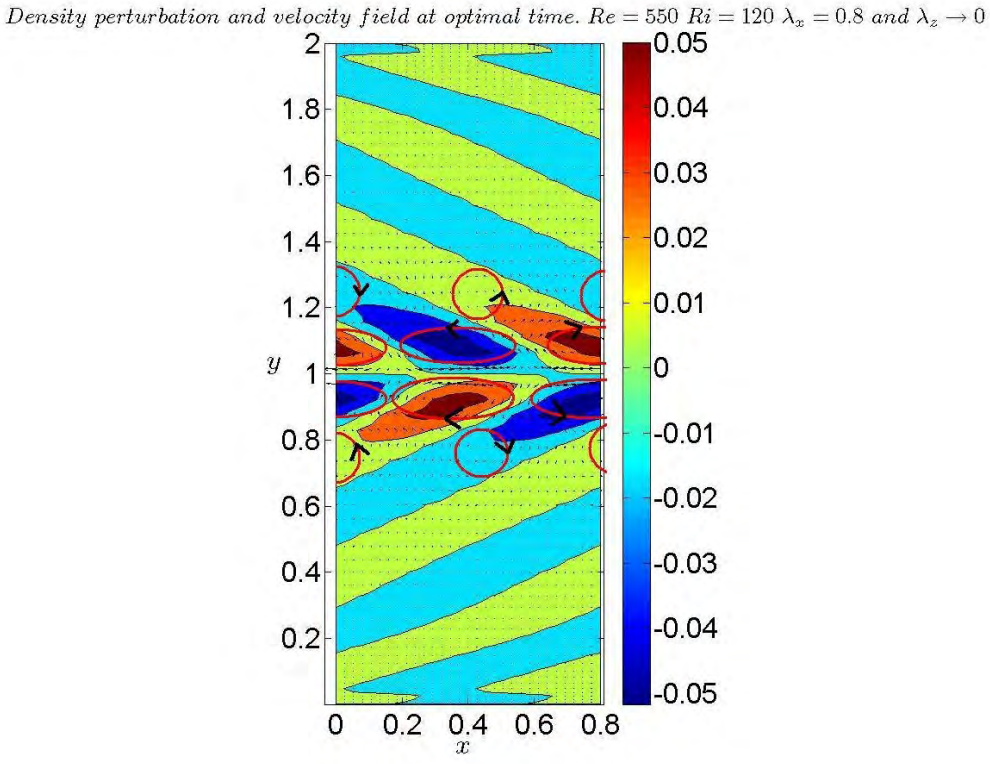

Figure 3-23: Perturbation velocity field and density fluctuations at Re=550, Ri=120, λ_x =0.8h and $\lambda_z \to \infty$

This last energy peak is of great importance because its evolution as the Richardson number increases tends to be the dominant one in the flow. Actually, when analysing the flow at Ri=480 it is found an unstable zone. Studying the energy distribution in the stable sizes near the instability zone, an analogous distribution between potential and kinetic energy is observed. Thus, it is concluded that it corresponds to the same phenomenon that appears at Ri=120 and λ_x =0.8h, and that grows exponentially at Ri=480. Therefore, this is the dominant structure at high Richardson numbers. In Figure 3-8 this zone is comprised around λ_x =2h and for values of λ_z >15h. This structure agrees remarkably well to the DNS by García-Villalba & Del Álamo (2008), where structures of around λ_x=2h are clearly observed (Figure 3-24).

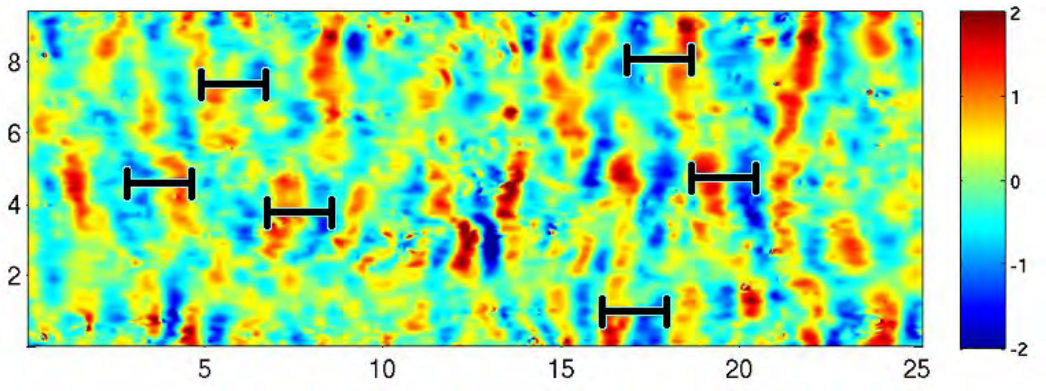

Figure 3-24: Vertical velocity in the centre of the channel in the x-z plane at Re=550 and Ri=480. Black markers are of size 2h and only emphasize that structures have a similar dimension. DNS picture by García-Villalba & Del Álamo (2008).

More information is given by analysing the eigenvalues in the unstable zone: with the imaginary part of the eigenvalues that zone can be determined with accuracy and with the real part of the eigenvalues can be checked the phase speed of the perturbation. Figure 3-25 shows that the phase speed, c_r, inside the unstable zone is around 29-30 u_τ, comparable to the bulk velocity U_b (defined as $U_b = \frac{1}{2}\int_{-1}^{1} U \, \mathrm{d}(y/h)$), which is 27.5u_τ. This speed of the dominant perturbation characterizes it, since the majority of the perturbation in other sizes propagates with a velocity similar to the maximum velocity of the mean flow in the centre of the channel, around 42 u_τ (not shown in the figure).

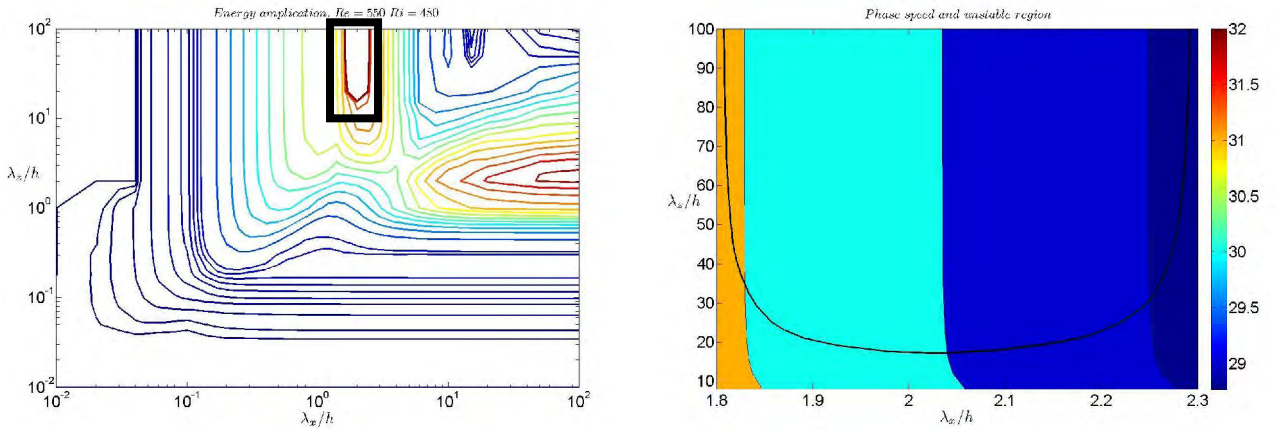

Figure 3-25: Figure on the right corresponds to the phase speed of the perturbation at Re=550 and Ri=480. The zone above the black curve corresponds to the unstable zone. Figure on the left is the same as Figure 3-8. with a black box which represents approximately the zone shown in the figure on the right.

3.8 Modes flow analysis.

The common appearance of the evolution of the energy in time for a stable flow with transient growth is the following:

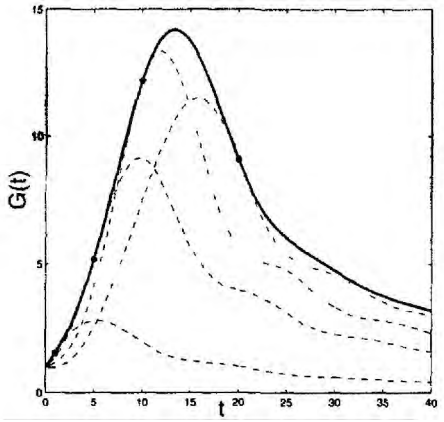

Figure 3-26: Amplification G(t) for Poiseuille flow with Re=1000, a=1 (solid line) and growth curves of selected initial conditions (dashed lines). Figure taken from Schmid & Henningson (2001)

It is important to keep in mind that throughout this work we have been making use only of the maximum value of the energy amplification, G_{max}, and the initial condition that yields it, and not the curve itself of the evolution of G with time. That curve represents the maximum possible energy amplification, which for each instant in time is optimized over all possible initial conditions with unit energy norm. The initial condition that optimizes the amplification factor might be different for different times so that G(t) should be thought of as the envelope of the energy evolution of individual initial conditions with unit energy norm. However, looking at the velocity and density fields at each concrete instant of time it is found a great similarity between all the points of the curve G(t). Therefore, it is concluded that the perturbations which form the envelope of the curve of maximum possible amplification belong to a same family that slightly evolved.

Nevertheless, in the stratified turbulent channel flow it has been observed in some combinations of λ_x and λ_z a more complex behaviour. Instead of the classical shape of G(t) with one family mode, two family modes have been noticed, as figure 3-27 shows:

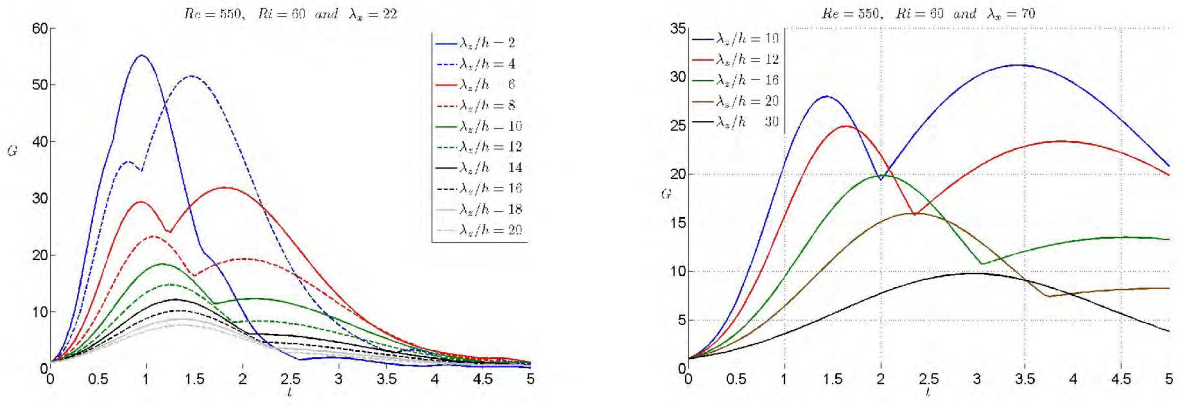

Figure 3-27: Maximum energy amplification in function of time for a fixed λ_x and several λ_z at Ri=60 and Re=550. Figure on the left corresponds to λ_x =22 and figure on the right to λ_x=70.

When plotting the contours of optimal time, this mode change can be predicted since a leap on the time for maximum energy amplification occurs. It goes unnoticed in the energy maps because there is no abrupt difference in energy when the transition of modes happens but a smooth evolution. On the other hand, time maps are the ideal way of searching this behaviour: the leap in time, which is remarkable (see figure 3-27), is seen as peaks in time contours. This shape of the map can be clearly observed in Figure 3-28, where these peaks are highlighted using red circles. The transition between the two modes is not just a matter of speed of the perturbation that reaches the maximum energy amplification, but a matter of the perturbation itself, whose velocity and density fields change from one to another. This fact leads us to consider both maximum in the curve of G(t), as part of two different family modes, each of one with its characteristic main perturbation. An example can be seen in Figures 3-29 and 3-30. There the case of Re=550, Ri=60 and λ_x =30h has been analysed. It is observed an abrupt change of the optimal time from around λ_z =10h to λ_z =12h which entails two different flow behaviours. The first one composed by two pair of counter-rotating vortices and that, moreover, are situated one in the upper half and the other in the bottom half setting up a barrier in the centre of the channel between both halves. And the second perturbation, where this barrier has disappeared, presents, on the other hand, a structure of internal waves in the middle of the channel. Despite this different behaviour, no significant differences in the distribution of energy (in kinetic and potential energy) have been found in all the cases tested.

These differences in time also entail a difficulty in computation, since it is necessary to delimit properly the range of times where the maximum is searched. It can occur than a local maximum in G is taken as the global one. This error must be avoided. Therefore, it is essential to be specially careful in selecting the range of times.

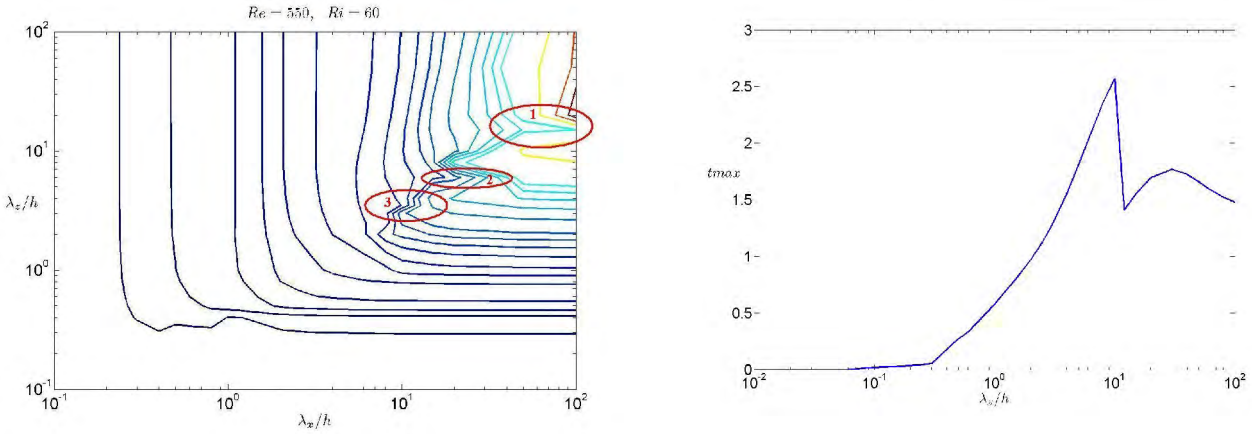

Figure 3-28: Figure on the left represents contours of optimal time for maximum energy amplification at Re=550 and Ri=60 in the (λ_x /h, λ_z/h) plane. Figure on the right represents the concrete case of λ_x =30h.

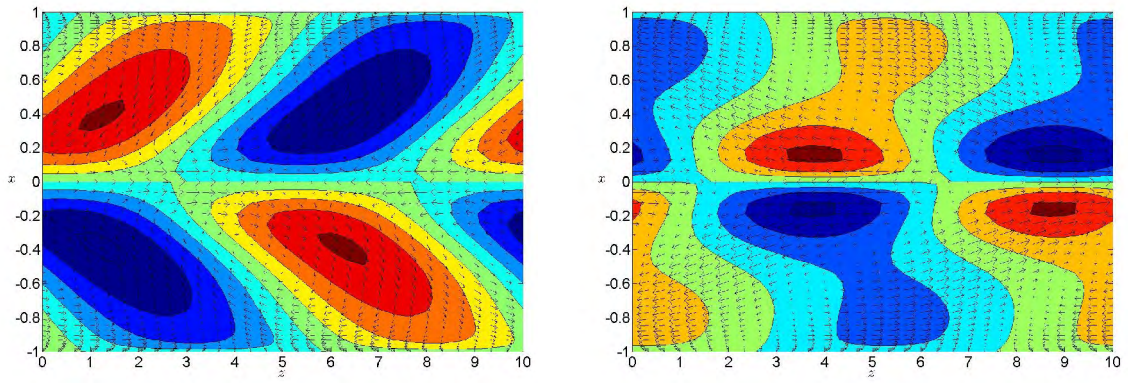

Figure 3-29: Velocity field (arrows) and density fluctuations (coloured levels) at Re=550, Ri=60, λ_x=30h and λ_z=10h. Figure on the left is the initial perturbation and figure on the right the perturbation at optimal time.

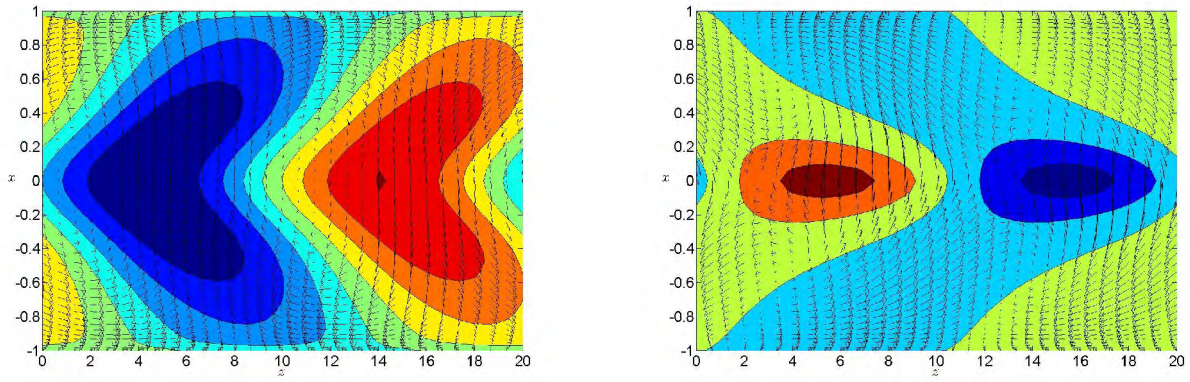

Figure 3-30: Velocity field (arrows) and density fluctuations (coloured levels) at Re=550, Ri=60, λ_x=30h and λ_z=20h. Figure on the left is the initial perturbation and figure on the right the perturbation at optimal time.

Chapter 4.- Conclusions and recommendation for further work.

Stably-stratified turbulent flow in a channel has been studied using linear stability analysis. A Matlab code for the resolution of the linear model has been developed in order to investigate the behaviour of this kind of flows. The results are compared to Direct Numerical Simulations (DNS) carried out by García-Villalba & Del Álamo (2008). Good agreement is found in the comparison, highlighting three main properties:

- At high Richardson numbers the prevalent structures in the flow have a size of $\lambda_x=2h$, which extends along the spanwise direction (see section 3.7).

- The width (λ_z) of the near-wall streaks decreases as the Richardson number increases (from around $\lambda_z=0.2h$ at $Ri_\tau=60$ to $\lambda_z=0.07h$ at $Ri_\tau=480$). See section 3.6.

- At high Richardson numbers vortical structures remain confined in the upper half or the bottom half of the channel, without crossing the centre of the channel (see section 3.4)

These results show that the linear model is able to capture approximately the development of perturbations that yields some of the dominant structures in a stratified turbulent channel flow.

The method used in this work, based on Schmid and Henningson (2001), enables us to compute the perturbation velocity field and density fluctuations, both at the initial and optimal time, as well as the maximum energy amplification in function of time and its distribution in components of the kinetic and potential energy. Moreover, the real part of the eigenvalues-solution reveals the phase speed at which the optimal perturbation travels.

In order to exploit all the advantages of this method, the future work based on these procedures might be oriented in the way of:

- Generalizing the analytical approximation of the turbulent eddy viscosity and thermal diffusivity to any Reynolds and Richardson number (as the Cess formula does for the turbulent unstratified flow). Thus, this method become independent of the DNS profiles and is able to explore a wide range of new cases varying the two parameters (Re and Ri). In the present work cases analyzed are restricted to the DNS cases carried out by García-Villalba & Del Álamo (2008)

- Generalizing to other type of flows (not only channel flows). As this method works, experimental profiles of other flows could be taken and implemented in the code to study its linear properties.

Bibliography

BATCHELOR, G.K. 1967 *An introduction to Fluid Dynamics*. Cambridge University Press

BIAU, D. and BOTTARO, A. 2004 The effect of stable thermal stratification on shear flow stability. *Phys. Fluids* 16, 4742-4775

BOYD, J.P. 2000 *Chebyshev and Fourier Spectral Methods*. DOVER Publications, New York

BUTLER, K.M. and FARREL, B.F. 1992 Three-dimensional optimal perturbations in viscous shear flows. *Phys. Fluids* 4, 1637-1650

CAULFIELD, C.P. and PELTIER W.R. 2000 The anatomy of the mixing transition in homogeneous and stratified free shear layer. *J. Fluid. Mech.* 413, 1-47

CESS, R.D. 1958 A survey of the literature on heat transfer in turbulent tube flow. *Westinghouse Research Rep*. no 8-0529-R24

CHEW, J.W. and HILLS, N.J. 2007 Computational fluid dynamics for turbomachinery internal air systems. *Phil. Trans. R. Soc. A* 365, 2587-2611

DEL ALAMO, J.C. and JIMENEZ, J. 2003 Spectra of the very large anisotropic scales in turbulent channels. *Phys. Fluids* 15, L41-L44

DEL ALAMO, J.C. and JIMENEZ, J. 2006 Linear energy amplification in turbulent channels. *J. Fluid Mech*. 559, 205-213

DEL ALAMO, J.C., JIMENEZ, J, ZANDONADE, P. and MOSER, R.D. 2004 Scaling of the energy spectra of turbulent channels. *J. Fluid Mech*. 500, 135-144

DRAZIN, P.G. and REID, W.H. 1981 *Hydrodynamic Stability*. Cambridge Universtiy Press

DRAZIN, P.G. 2002 *Introduction to Hydrodynamic Stability*. Cambridge University Press

GAGE, K.S. and REID, W.H. 1968 The stability of thermally stratified plane Poiseuille flow. *J. Fluid Mech*. 33, 21-32

GARCIA-VILLABA, M. and DEL ALAMO, J.C. 2008 DNS of stably-stratified turbulent channel flow. In preparation

GUSTAVSSON, L.H. 1991 Energy growth of 3-dimensional disturbances in plane Poiseuille flow. *J. Fluid Mech.* 224, 241-260

HERBERT, T. 1977 Die Neutrale Fläche der ebenen Poiseuille-Strömung. Stuttgart.

JIMENEZ, J. 2007 Recent developments on wall-bounded turbulence. *Rev. R. Acad. Cien. Serie A. Mat*. 101, 187-203

KUNDU, K.K. and COHEN, I.M. 2002 *Fluid Mechanics. Second Edition*. Academic Press

MACK, L.M. 1976 A numerical study of the temporal eigenvalue spectrum of the Blasius boundary layer. *J. Fluid Mech.* 73, 497-520

ORSZAG, S.A. 1971 Accurate solution of the Orr-Sommerfeld stability equation. *J. Fluid Mech*. 50, 689-703

PATEL, V.C. and HEAD, M.R. 1969 Some observations on skin friction and velocity profiles in fully developed pipe and channel flows. *J. Fluid Mech.* 38, 181-&

REYNOLDS, W.C. & HUSSAIN, A. K. M. F. 1972 The mechanics of an organized wave in turbulent shear flow. Part 3. Theoretical models and comparisons with experiments. *J. Fluid Mech.* 54, 263-288

REYNOLDS, W.C. and TIEDERMAN, W.G. 1967 Stability of turbulent channel flow, with application to Malkus's theory. 1967 *J. Fluid Mech*. 27, 253-272

ROBINSON, S.K. 1991 Coherent Motions in the Turbulent Boundary Layer. *Ann. Rev. Fluid Mech.* 1991, 23, 601-639

SCHMID, P.J. and HENNINGSON, D.S. 2001 *Stability and Transition in Shear Flows.* Springer-Verlag, New York

SMITH, C.R. and METZLER, S.P. 1983 The characteristics of low-speed streaks in the near-wall region of a turbulent boundary layer. *J. Fluid Mech*. 129, 27-54

SMYTH, W.D. MOUM, J.N. and CALDWELL, D.R. 2001 The efficiency of mixing in turbulent patches: interferences from direct simulations and microstructure observations. *J. Phys. Ocean*. 31, 1969-1992

THORPE, S.A. 2005 *The turbulent* ocean. Cambridge University Press

TUCKER, P.G. 2007 Introduction. Computational aerodynamics. *Phil. Trans. R. Soc. A* 365, 2379-2388

TURNER, J.S. 1973 *Buoyancy Effects in Fluids*. Cambridge University Press

Appendix A.- Chebyshev Discretization

In this appendix some mathematical properties and techniques that have been needed to implement successfully the linearized Navier-Stokes equation in the Matlab code are commented. The equations for laminar flow have been considered in this appendix with the intention of making the explanation clearer, since turbulent equations only differs in new terms added (that are treated in the same way) and do not give any more relevant information about the mathematical procedure. A brief definition of Chebyshev series is given, then it is detailed the way to discretize Orr-Sommerfeld and Squire equations, as well as how to implement both in the complete problem. It is also detailed the normalization in energy of the eigenfunctions, a fundamental previous step to be able to compare transient growth in the different cases. Finally, some Chebyshev properties used in this study are given.

A.1 Chebyshev Series

Spectral methods have had a significant impact on the accurate discretization of both initial value and eigenvalue problems. Especially in a bounded domain, as the channel flow is, the use of Chebyshev polynomials has been advantageous. All the stability calculation computed for this study have been obtained by a Chebyshev discretization of the inhomogeneous coordinate direction. A complete and broad description of Chebyshev spectral methods is given in Boyd (2000)

Any function f(y) can be approximated by a Chebyshev expansion:

$$f(y) = \sum_{n=0}^{\infty} a_n T_n(y) \approx \sum_{n=0}^{N} a_n T_n(y) \qquad \text{(A.1)}$$

where T_n are the Chebyshev polynomials and a_n are the coefficients, typical from each function f(y).

Chebyshev polynomial can be defined in many ways, for example, in terms of trigonometric functions:

$$T_n \equiv \cos(n\theta) \quad \text{where} \quad y = \cos(\theta) \qquad \text{(A.2)}$$

Throughout this study Chebyshev polynomials have been evaluated in the locations $y_j = \cos(\frac{j\pi}{N})$ known as the Gauss-Lobatto points. Equations have been discretized in this way because it has the advantage of having more nodes near the walls (y±1) where the gradients of velocity or density are more marked.

A.2 Discretization of Orr-Sommerfeld Equation

The Orr-Sommerfeld equation reads

$$\left[(U-c)\left(D^2-k^2\right)-U''-\frac{1}{i\alpha\,\mathrm{Re}}\left(D^2-k^2\right)^2\right]\tilde{v}=0 \tag{A.3}$$

After some algebraic work, it reaches the form

$$(-Uk^2-U''-\frac{k^4}{i\alpha\,\mathrm{Re}})\tilde{v}+(U+\frac{2k^2}{i\alpha\,\mathrm{Re}})\tilde{v}''-\frac{1}{i\alpha\,\mathrm{Re}}\tilde{v}'^{v}=c(\tilde{v}''-k^2\tilde{v}) \tag{A.4}$$

Eigenfunctions and their derivatives are expanded in a Chebyshev series

$$\begin{aligned}\tilde{v}(y)&=\sum_{n=0}^{N}a^{(\tilde{v})}{}_nT_n(y)\\ \tilde{v}''(y)&=\sum_{n=0}^{N}a^{(\tilde{v})}{}_nT''_n(y)\\ \tilde{v}'^{v}(y)&=\sum_{n=0}^{N}a^{(\tilde{v})}{}_nT'^{v}{}_n(y)\end{aligned} \tag{A.5}$$

Introducing these approximations in the Orr-Sommerfeld equation, it reads now as follows

$$\sum_{n=0}^{N}\left[(-Uk^2-U''-\frac{k^4}{i\alpha\,\mathrm{Re}})T_n+(U+\frac{2k^2}{i\alpha\,\mathrm{Re}})T_n''-\frac{1}{i\alpha\,\mathrm{Re}}T_n'^{v}\right]a^{(\tilde{v})}{}_n=c\sum_{n=0}^{N}(T_n''-k^2T_n)a^{(\tilde{v})}{}_n \tag{A.6}$$

with the boundary conditions

$$\begin{aligned}\tilde{v}(\pm1)&=0\\ \tilde{v}'(\pm1)&=0\end{aligned}\Rightarrow\begin{cases}\sum_{n=0}^{N}a^{(\tilde{v})}{}_nT_n(\pm1)\\ \sum_{n=0}^{N}a^{(\tilde{v})}{}_nT_n'(\pm1)\end{cases} \tag{A.7}$$

It takes then the matrix form

$$\mathbf{A_{11}a^{(\tilde{v})}}=c\mathbf{B_1a^{(\tilde{v})}} \tag{A.8}$$

where an Eigenvalue problem can be recognised.

Following Schmid & Henningson (2001) , the implementation of the two boundary conditions in the variable $\tilde{v}$ is made by using the first and last row of B, and, for the two remaining boundary conditions in its derivative, the second and next-to-last row of B are used. The same rows in the matrix A can be chosen as a complex multiple of the corresponding rows in B. By carefully selecting this complex multiple, the spurious modes associated with the boundary conditions can be mapped to an arbitrary location in the complex plane. In the laminar flow this multiple has been chosen with a value of -200i, which is suitable to keep spurious modes away from the least damped eigenvalues (Schmid & Henningson, 2001); and in the turbulent flow this multiple has

been taken as the maximum between the Reynolds number and Re/λ_z in the way $-\max(\mathrm{Re},\mathrm{Re}/\lambda_z)i$ (where i is in both cases the imaginary number).

A.3 Discretization of Squire Equation

The process of the Discretization of Squire Equation is analogous to the Orr-Sommerfeld one. Squire equation reads

$$\left[i\alpha\left(U-c\right)-\frac{1}{\mathrm{Re}}\left(D^2-k^2\right)\right]\tilde{\eta}=-i\beta U'\tilde{v} \tag{A.9}$$

After some algebraic work, it reaches to the form

$$\left(i\alpha U+\frac{k^2}{\mathrm{Re}}\right)\tilde{\eta}-\frac{1}{\mathrm{Re}}\tilde{\eta}''+i\,\beta U'\tilde{v}=i\alpha c\tilde{\eta} \tag{A.10}$$

Eigenfunctions are expanded in a Chebyshev series

$$\tilde{\eta}(y)=\sum_{n=0}^{N}a_n^{(\tilde{\eta})}T_n \tag{A.11}$$

Introducing these approximations in the Squire equation, it reads now as follows

$$\sum_{n=0}^{N}\left\{\left[\left(i\alpha U+\frac{k^2}{\mathrm{Re}}\right)T_n-\frac{1}{\mathrm{Re}}T_n''\right]a_n^{(\tilde{\eta})}+\left(i\beta U'T_n\right)a_n^{(\tilde{v})}\right\}=c\sum_{n=0}^{N}\left(i\alpha T_n\right)a_n^{(\tilde{\eta})} \tag{A.12}$$

with the boundary conditions

$$\tilde{\eta}(\pm1)=0\Rightarrow\sum_{n=0}^{N}a_n^{(\tilde{\eta})}T_n(\pm1)=0 \tag{A.13}$$

The equation above can be written in the compact form

$$\mathbf{A}_{22}\mathbf{a}^{(\tilde{\eta})}+\mathbf{A}_{21}\mathbf{a}^{(\tilde{v})}=c\mathbf{B}_2\mathbf{a}^{(\tilde{\eta})} \tag{A.14}$$

A.4 Complete Problem. Eigenvalue Problem

Orr-Sommerfeld and Squire equations can be put together in a matrix form. The different blocks are combined as follows

$$\begin{bmatrix}\mathbf{A}_{11} & \mathbf{0}\\ \mathbf{A}_{21} & \mathbf{A}_{22}\end{bmatrix}\begin{Bmatrix}\mathbf{a}^{(\tilde{v})}\\ \mathbf{a}^{(\tilde{\eta})}\end{Bmatrix}=c\begin{bmatrix}\mathbf{B}_1\\ \mathbf{B}_2\end{bmatrix}\begin{Bmatrix}\mathbf{a}^{(\tilde{v})}\\ \mathbf{a}^{(\tilde{\eta})}\end{Bmatrix}\Rightarrow\mathbf{A}\hat{\mathbf{q}}=c\mathbf{B}\hat{\mathbf{q}}\Rightarrow\left[\mathbf{B}^{-1}\mathbf{A}-c\mathbf{I}\right]\hat{\mathbf{q}}=\mathbf{0} \tag{A.15}$$

An Eigenvalue problem is found. The Eigenfunctions are the set of the Chebyshev coefficients of the wall-normal velocity and normal vorticity functions $\hat{\mathbf{q}}=\begin{Bmatrix}\mathbf{a}^{(\tilde{v})}\\ \mathbf{a}^{(\tilde{\eta})}\end{Bmatrix}$

A.5 Energy Weight Matrix and Energy Inner Product

When Transient Growth is studied, one of the first steps to take is rescaling eigenfunctions so the kinetic energy of each one is unitary. Here it is explained how it has been computed the matrix to normalize the eigenfunctions, taken into account the Chebyshev Discretization developed above.

The kinetic energy can be written in terms of the Chebyshev coefficients of the disturbance variables as follows

$$E = \frac{1}{2}\int_{-1}^{1}\left(\left|\tilde{u}\right|^2 + \left|\tilde{v}\right|^2 + \left|\tilde{w}\right|^2\right)dy = \frac{1}{2k^2}\int_{-1}^{1}\left(\left|D\tilde{v}\right|^2 + k^2\left|\tilde{v}\right|^2 + \left|\tilde{\eta}\right|^2\right)dy \tag{A.16}$$

Introducing the Chebyshev expansion

$$E = \frac{1}{2k^2}\int_{-1}^{1}\left(\left|\sum_{n=0}^{N} {}^{1}a^{(\tilde{v})}{}_{n}{}^{1}T_n(y)\right|^2 + k^2\left|\sum_{n=0}^{N} a^{(\tilde{v})}{}_{n}T_n(y)\right|^2 + \left|\sum_{n=0}^{N} a_n^{(\tilde{\eta})}T_n\left(y\right)\right|^2\right)dy \tag{A.17}$$

Using the Chebyshev Properties explained below and writing the expression in a matrix form

$$E = \frac{1}{2k^2}\mathbf{v^H}\begin{pmatrix}\mathbf{D^H C D + k^2 C} & \mathbf{0}\\ \mathbf{0} & \mathbf{C}\end{pmatrix}\mathbf{v} = \frac{1}{2k^2}\mathbf{v^H M v} = \frac{1}{2k^2}\mathbf{v^H W^H W v} \tag{A.18}$$

Therefore, eigenfunctions normalization is as follows

$$\hat{\mathbf{q}}_{E=1} = \frac{\hat{\mathbf{q}}}{\frac{1}{\sqrt{2k^2}}\left\|\mathbf{W}\hat{\mathbf{q}}\right\|_2} \tag{A.19}$$

Notation $\left\|\square,\square\right\|_E$ will be used for the energy inner product, which is defined as

$$\left\|\mathbf{v_1}, \mathbf{v_2}\right\|_E^2 = \frac{1}{2k^2}\mathbf{v_1^H W^H W v_2} \tag{A.20}$$

In the case of a stratified flow it must be taken into account in the energy matrix not only the kinetic energy but also the potential one. The expression of the total energy is as follows:

$$E = \frac{1}{2}\int_{-1}^{1}\left(\left|\tilde{u}\right|^2 + \left|\tilde{v}\right|^2 + \left|\tilde{w}\right|^2\right)dy + \int_{-1}^{1}\left|\frac{Ri}{\overline{\rho}'}\tilde{\rho}^2\right|dy \tag{A.21}$$

and in the matrix form:

$$E = \frac{1}{2k^2}\begin{pmatrix}\tilde{v} & \tilde{\eta} & \tilde{\rho}\end{pmatrix}\begin{pmatrix}\mathbf{D^H C D + k^2 C} & \mathbf{0} & \mathbf{0} \\ \mathbf{0} & \mathbf{C} & \mathbf{0} \\ \mathbf{0} & \mathbf{0} & 2k^2\frac{Ri}{\rho_0'}\mathbf{C}\end{pmatrix}\begin{pmatrix}\tilde{v} \\ \tilde{\eta} \\ \tilde{\rho}\end{pmatrix} \qquad \text{(A.22)}$$

that can be decomposed in the same way as above.

A.6 Some Chebyshev Series Properties

The derivatives of the expanded functions can be computed in two different ways: by taking derivative of the Chebyshev polynomials, or, on the contrary, by taking derivative of the Chebyshev coefficients, that is to say, $f'(y) = \sum_{n=0}^{N} a_n T_n'(y) = \sum_{j=0}^{2K\,1} a_j' T_j(y)$ (see below).

A.6.1 Chebyshev Polynomials Derivative

$$f^i(y) = \sum_{n=0}^{N} a_n T_n^i(y) \qquad \text{(A.23)}$$

$$T_0^i(y_j) = 0 \qquad \text{(A.24)}$$

$$T_1^i(y_j) = T_0^{i-1}(y_j) \qquad \text{(A.25)}$$

$$T_2^i(y_j) = 4T_1^{i-1}(y_j) \qquad \text{(A.26)}$$

$$T_n^i(y_j) = 2nT_n^{i-1}(y_j) + \frac{n}{n-2}T_{n-1}^i(y_j) \qquad n = 3,4,... \qquad \text{(A.27)}$$

A.6.2 Chebyshev Coefficients Derivative (Herbert 1977)

$$f^i(y) = \sum_{j=0}^{2K\,1} a_j^i T_j(y) \qquad \text{(A.28)}$$

$$a_j^i = \sum_{k=j+1}^{2K\,2} d_{jk}^1 a_k^{i-1} = ... = \sum_{k=j+1}^{2K\,2} d_{jk}^i a_k \qquad \text{(A.29)}$$

$$d_{jk}^i = 0 \qquad for\ \ k < j+i \qquad \text{(A.30)}$$

$$d_{jk}^1 = 2k \qquad \text{(A.31)}$$

$$d_{jk}^2 = k(k^2 - j^2) \qquad \text{(A.32)}$$

$$d_{jk}^3 = \frac{k}{4}\left[(k^2-1)^2 - 2k^2j^2 + j^2(j^2-2)\right] \qquad \text{(A.33)}$$

$$d_{jk}^4 = \frac{k}{24}\left[k^2(k^2-4)^2 - 3k^2j^2(k^2-j^2) - j^2(j^2-4)^2\right] \qquad for\quad k \geq j+i \qquad \text{(A.34)}$$

$\sum^1$ the first term of the series has a factor ½

$\sum^{2}$ the index summation increases in 2

A.6.3 Orthogonality of Chebyshev Polynomials

Chebyshev polynomials satisfy the following orthogonality relation on the form

$$C_{ij} = \int_{-1}^{1} T_i T_j dy = \begin{cases} 0 & for\ \ i+j\ odd \\ \dfrac{1}{1-(i+j)^2} + \dfrac{1}{1-(i-j)^2} & for\ \ i+j\ even \end{cases} \tag{A.35}$$